Experimental Investigation of the Hydrodynamics in a Liquid–Solid Riser

Shantanu Roy, Abdenour Kemoun, M. H. Al-Dahhan, and M. P. Dudukovic

Chemical Reaction Engineering Laboratory, Dept. of Chemical Engineering, Washington University, St. Louis, MO 63130

Liquid–solid fluid dynamics has been investigated in a 6-in. (0.15 m) "cold-flow" circulating fluidized bed riser using non-invasive flow monitoring methods. Gamma-ray computed tomography (CT) was used to measure the time-averaged cross-sectional solids volume fraction distributions at several elevations. The time-averaged mean and "fluctuating" solids velocity fields were quantified using the computer-automated radioactive particle tracking (CARPT) technique. The experimental equipment, protocol of implementation, and data analysis have been discussed briefly, with particular emphasis on the specific features in the use of these techniques for studying high-density turbulent flows as in a liquid–solid riser. The experimental study examines nine operating conditions, that is, three liquid superficial velocities and three solids flow rates. The solids holdup profile is found to be relatively uniform across the cross section of the riser, with marginal segregation near the walls. The time-averaged solids velocity profiles are found to have a negative component at the walls, indicating significant solids backmixing. Detailed characterization of the solids velocity fields in terms of RMS velocities, kinetic energies, Hurst exponents, residence time distributions, trajectory length distributions, dispersion coefficients, and so forth are presented. Comparative and symbiotic analyses of the results were used to develop a coherent picture of the solids flow field. In addition, the work also serves to demonstrate the power and versatility of these flow-imaging techniques in studying highly turbulent and opaque multiphase systems. © 2005 American Institute of Chemical Engineers *AIChE J,* 51: 802–835, 2005
Keywords: liquid–solid riser, CARPT, tomography, solids volume fraction, solids flow pattern

Introduction

Alkylation processes have been, and continue to be, a very important class of industrial reactions. The world market and consumption patterns of both aliphatic and aromatic alkylates are rapidly growing, with an average annual growth rate of 4–5% in worldwide demand in the last decade (Roy, 2000; Roy

and Dudukovic, 2001b). This growth has been prompted by increasingly stringent gasoline standards enacted around the world in recent years, leading to a surge in demand for motor fuel alkylate, which is an important additive in reformulated gasoline (RFG). The demand for linear alkylbenzene (which is an aromatic alkylate and the most widely used component of industrial and household detergents) is also on the rise (Corma and Martinez, 1993; Liang et al., 1995, 1996, 1997a,b,c; Roy, 2000; Vora et al., 1990).

Conventionally, the production of LAB (linear alkylbenzene) and other alkylated olefins and aromatics was achieved through the use of strong liquid phase acids (homogeneous catalyst), such as hydrofluoric acid and sulfuric acid (Corma and Martinez, 1993; Edmonds, 1981; Thomas, 1970; Vora et

---
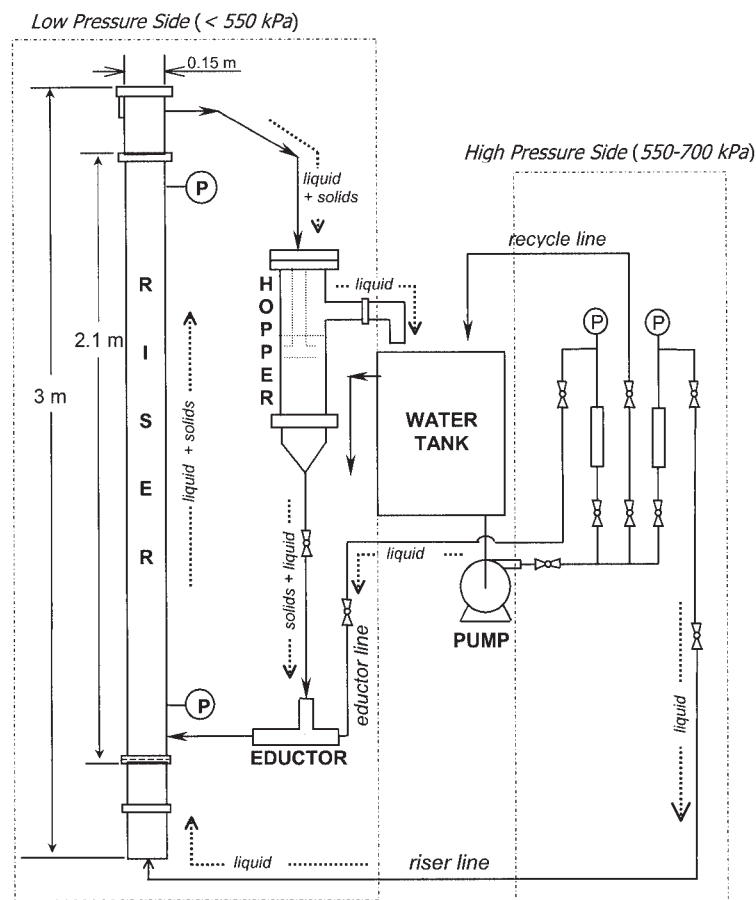
Figure 1. Liquid–solid circulating fluidized bed setup.

al., 1990). The problems associated with handling corrosive acids, equipment corrosion, hazards to operating personnel, and environmental threats posed by both the acids and by-products made these processes unfavorable.

The search for more environmentally benign processes for alkylation, with improved selectivity and lower turnover times, has led to the emergence of solid-acid catalyzed technologies, with liquid–solid circulating fluidized beds being the reactors of choice (Vora et al., 1990). In these proposed processes, the solid-acid zeolites (such as zeolite/BF_3: Corma and Martinez, 1993; Weitkamp, 1980), or solid superacids on inorganic and organic supports (Corma and Martinez, 1993) produce better process selectivity and yield of the desired product with turnover times averaging around 1 min (as opposed to 20–30 min in the earlier homogeneous acid-catalyzed processes). However, these highly active solid catalysts are also rapidly deactivated and need to be periodically recycled to ensure continuous operation. A liquid–solid circulating fluidized bed is one of the preferred reactor options, which allows the solid-acid catalyst particles to be recycled between the reactor (riser) zone and the regenerator zone. The hydrocarbon reactants are in liquid phase at high pressures and low temperatures, and flow concurrently upward with the catalyst particles in the riser, where the principal alkylation reaction takes place. A schematic process flow sheet and other process details have been presented elsewhere (Roy, 2000; Roy and Dudukovic, 2001b).

As with other multiphase reactors with moving catalysts, the reactor performance of liquid–solid circulating reactors is expected to be a strong function of the hydrodynamics, solids loading, and solids flow pattern in the riser (Carlos and Richardson, 1968; Chen et al., 1991; Di Felice, 1994, 1995; Kwauk, 1963, 1964; Liang et al., 1995, 1996, 1997a,b,c; Zheng and Zhu, 2001). The flow pattern under highly convective conditions is certainly expected to be chaotic and turbulent, with a high volume fraction of solids not necessarily uniformly distributed. Thus, a cold flow study, using the appropriate experimental tools is warranted. In this communication, we present the results from an extensive cold-flow experimental study of a laboratory-scale liquid solid riser. A few key results from this work were published by Roy and Dudukovic (2001b) in a article focused on the modeling aspects of the program. The present article discusses the complete experimental program detailing all the experimental techniques, methods, and findings.

Experimental Setup, Techniques, and Implementation

Liquid–solid riser setup

Figure 1 shows an overall schematic diagram of the experimental setup used in this work. Water served as the liquid phase and 2.5-mm-diameter glass beads (density = 2540 kg m^{-3}) were used as the dispersed solids phase. Continuous flow of both phases, at sufficient upstream pressure and liquid flow rate, was maintained to ensure steady-state operation of the

system. The setup was designed and adapted in such a way so that it was possible to conduct experiments using the existing computed tomography (CT) and computer-automated radioactive particle tracking (CARPT) platform at the Chemical Reaction Engineering Laboratory (CREL) at Washington University.

The riser setup consisted of a vertical Plexiglas® column, of total height of about 3 m with a 2.13 m section representing the developed flow in the riser section. Two inlet lines, one entering vertically below the 2.13 m section and the other entering horizontally a little above (0.22 m) the riser base (Figure 1), were used to deliver flows independent of each other to the riser. Solids (glass beads) entered the riser from the latter line, driven by the liquid phase (water), whereas the vertical line fed the remaining water to the riser. The solids and liquid flowed concurrently upward in the riser and exited through a specially constructed frustum whose diameter is reduced from 0.15 m to 0.05 m over a height of 0.36 m. An exit line (0.05 m diameter) conveyed the liquid–solid mixture from the head of the riser to the hopper, which maintained the inventory of the solids. The hopper had a wire mesh to separate the solids and liquid. The liquid (water) was conveyed back into the holding water tank, whereas the solids passed through the vertical pipe below the hopper into the solids eductor. Total water flow rate to the system was maintained using rotameters positioned in both water lines (Figure 1), the one to the eductor (referred to as the eductor line) and the other to the bottom of the riser (referred to as the riser line). The eductor was a "Venturi-like" device that directed solids flow into the riser. The functional relationship between the solids delivery rate and the motive water flow rate was independently established using radioactive tracing methods, and forms the subject of a related paper (Roy et al., 2001a).

The system operated in "variable inventory mode." Some of the liquid (water) was used to direct all of the solids flow through the eductor line (Figure 1), whereas the remainder liquid flowed through the riser line. Thus, the total flow rate of solids (entering only through the eductor line) and the total flow rate of liquid (entering through both the eductor and the riser lines) could be varied independently of each other. The recycle line returned the excess liquid being pumped into the riser setup to the holding tank. This ensured a steady pressure head at the eductor and riser inlets and stable operation of the loop. Further details of each unit in the setup, their construction, and assembly have been described elsewhere (Roy, 2000).

For characterizing the flow pattern of the solids phase, two kinds of measurements were critical: that of the solids volume fraction distribution and the solids velocity field. It has been recognized in multiphase flow research in the past decades (for example, Miller and Gidaspow, 1992) that both measurements in the same system are necessary for complete characterization of the flow pattern. In what follows, we describe in brief the methodology followed in this work for assessment of the solids holdup distribution and velocity fields, and a brief description of the setups. Details may be found in Roy (2000).

Computed tomography (CT)

A computed tomography (CT) setup for probing phase volume fractions in laboratory-scale multiphase reactors was previously developed, as reported in Kumar (1994). For this work,

the existing setup was suitably modified for studying the time-averaged solids-phase volume fraction in the liquid–solid riser setup shown in Figure 1. Figure 2 shows the schematic diagram of the setup, with the liquid–solid riser (Figure 1) positioned at the center of the CT scanner.

Transmission tomography is based on the principle that when a collimated beam of radiation is passed through any object, it loses intensity (becomes "attenuated") as a direct function of the density of the intervening medium. When the intervening medium is a multiphase system (such as the liquid–solid riser), its density depends linearly on the volume fraction of the phases. Thus a radiation attenuation measurement (called a "projection") may be used to "reconstruct" the volume fractions of the phases. In tomography for multiphase reactors (Kumar, 1994), a collimated beam of radiation is passed through the vessel of interest, *many* projection measurements are collected, and rigorous algorithms are used to reconstruct the *pointwise* distribution of phase volume fraction (Kak and Slaney, 1988; Kumar, 1994; Kumar and Dudukovic, 1997; Roy, 2000).

Figure 2 shows the setup with in the particular configuration of the liquid–solid riser study. Four threaded vertical guide rods on which a perfectly horizontal plate is positioned so as to allow its smooth vertical motion automated by gears. On this is fixed a "gantry" plate, and both plates have an aligned 2-ft-diameter circular opening at the center so as to allow concentric positioning of the reactor column being studied, the riser in this case. An elaborate column-positioning device (shown in Figure 2) that is fixed to the laboratory floor ensures perfect vertical alignment of the reactor column. On the gantry plate is stationed a 100-mCi lead-shielded Cs-137 source (half-life of around 37 years) and an array of NaI(Tl) scintillation detectors that are positioned across the column diameter facing the source. The whole assembly (source plus detector array) rotates around the column during the data-acquisition process, with the motion accurately timed and controlled by stepper motors. The total scanning time, over which the solids holdup distribution in the riser is thus averaged, is a little less than 2 h. For the image reconstruction, the iterative estimation–maximization (E-M) algorithm (Lange and Carson, 1984) is used, the implementation of which for the CREL scanner has been discussed by Kumar (1994) and Roy (2000). As a result of the data acquisition, one obtains a vector of projection measurements, with each element of the vector referenced by the angle of the view, and the angular position within a view. The output of the algorithm is a two-dimensional array of time-averaged total attenuation coefficient $\langle \mu_{eff}(x, y) \rangle$, as a function of location (x, y) on a plane. From these data, one backs out the time-averaged solids holdup at each location (pixel) coordinate (x, y) on the plane of interest

$$\langle \mu_{eff}(x, y) \rangle = \mu_l \langle \varepsilon_l(x, y) \rangle + \mu_s \langle \varepsilon_s(x, y) \rangle \qquad (1a)$$

$$\langle \varepsilon_s(x, y) \rangle = \frac{\langle \mu_{eff}(x, y) \rangle - \mu_l}{\mu_s - \mu_l} \qquad (1b)$$

Computer-automated radioactive particle tracking (CARPT)

CARPT is a non-invasive flow-mapping technique that is based on the principle of tracking the motion of a single
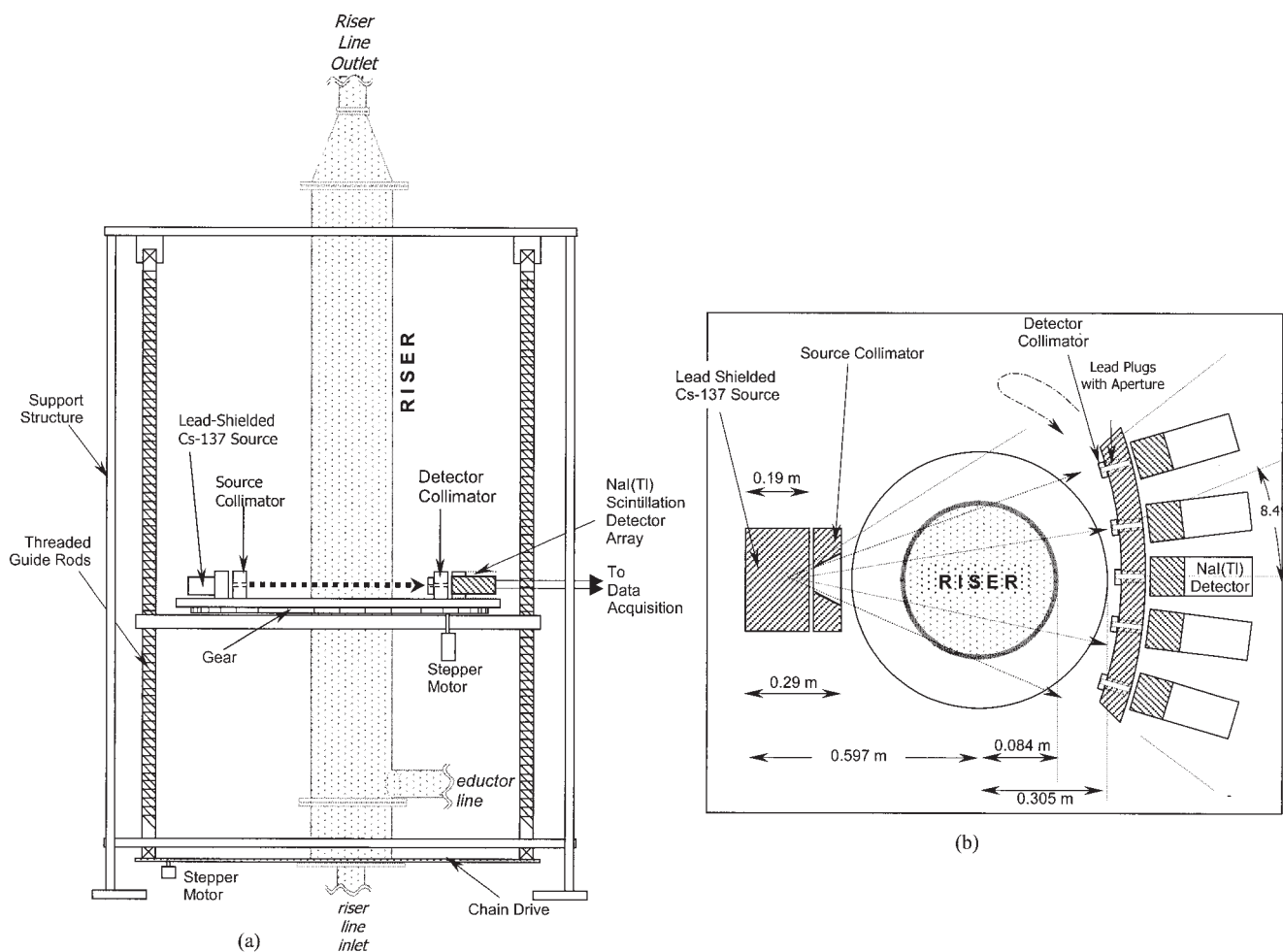
**Figure 2. CT scanner with riser in position.**

(a) Plan view; (b) top view.

particle as a marker of a typical element of the phase whose velocity field is to be mapped (for example, Degaleesan, 1997; Devanathan, 1991; Devanathan et al., 1996; Larachi et al., 1994, 1997; Lin et al., 1985). The tracer isotope chosen is normally a gamma-ray (highly penetrating radiation) emitter, so that it is possible to probe the flows even with a high volume fraction of particles. The process of tracking the tracer particle is completely automated and the data are acquired at a high enough frequency so that successive instantaneous positions of the particle are recovered with fidelity. Because the tracer particle is "designed" to represent the phase of interest, by collecting statistically significant data it is possible to extract the time-averaged velocity fields and mixing patterns of the traced phase in opaque systems. The experiment yields a "Lagrangian" trace of the tracer particle as a function of time, which allows for extracting information about the flow field in a multitude of ways, as will be discussed later.

As of now, CARPT is not an "off-the-shelf" technique and thus the practical implementation of the measurement is specific to the multiphase reactor system under study. Figure 3a shows a schematic representation of the CARPT implementation on the liquid–solid riser. An array of NaI(Tl) scintillation detectors are positioned all around the column to detect the

tracer particle (which is designed to mimic the solid-phase particles in a congeneric manner) position. As the solid particles circulate in the closed loop, so does the tracer particle, which periodically passes through the zone of interrogation of the detectors (Figure 3a).

For the current experiments the glass particles that form the solids inventory were obtained from Cataphote, Inc. (Jackson, MS). The stated specific gravity of these glass beads was 2.54, and the mean diameter of the particles was 2.5 ± 0.1 mm. Before conducting the CARPT experiments, both the exact mean size and mean density (2.49 g cm^{-3}) of the particles were established with carefully designed settling experiments (performed by following the unhindered terminal velocity of the tracer particle in a large glass vessel and back-calculating the effective mean density of the particle) (Roy, 2000). The tracer isotope was fashioned out of a 2.5-mm-diameter aluminum ball, with a hole 1.0 mm in diameter and 1.0 mm in height carefully drilled into it. In parallel, 0.403 mg scandium-45 isotope (nonradioactive) was carefully weighed out in a Cahn® C-35 microbalance. This was quartz-encapsulated in vacuum and sent for irradiation to the Research Reactor Facility, University of Missouri, Columbia nuclear reactor. Under an irradiation neutron flux of 8.0×10^{13} neutrons cm^{-2} s^{-1}, the
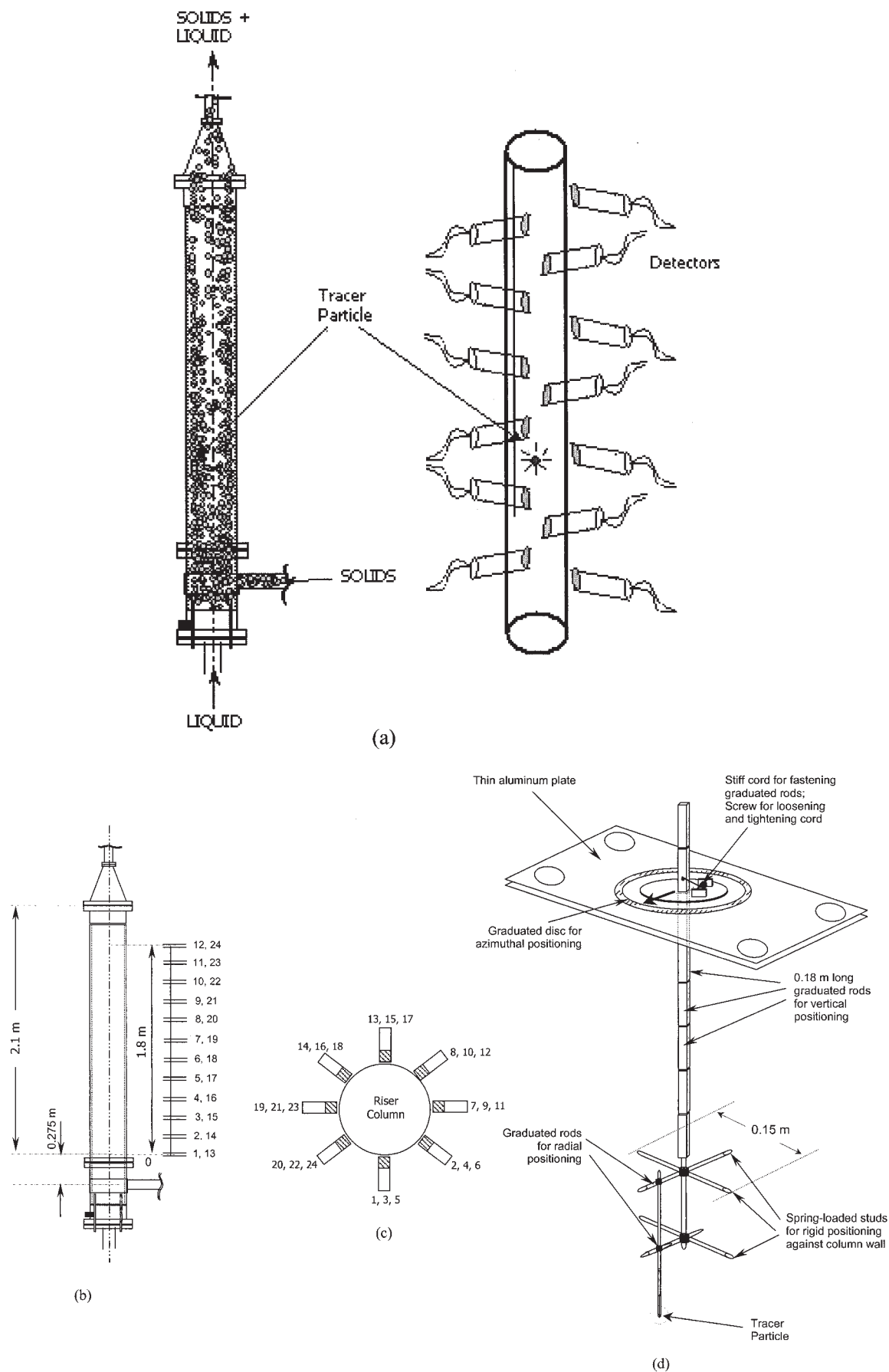
Figure 3. CARPT configuration around the liquid–solid riser.

(a) Riser with solids inventory and tracer particle. Detectors sensitive to tracer particle location, positioned around column at strategic locations. (b) Schematic representation of detector positioning around riser column. Front view. (c) Top view (not to scale). (d) Schematic of tracer particle positioning device, used for calibration.

irradiation took around 2 h and transmuted the scandium-45 to radioactive scandium-46 (half-life of 83 days). The resulting isotope, in granular form, with total strength of 290 μCi, was carefully introduced into the aluminum ball with the help of tweezers and under a magnifying glass. The open orifice in the ball was sealed with epoxy resin and Superglue®. Finally, the excess glue was filed off to produce a smooth outer surface. A thin coat of red paint was applied to make the particle completely wettable and for easy recognition of the tracer particle during the experiment. The effective density of the resulting particle was ensured to 2.49 $\pm$ 0.01 g cm^{-3}.

For the CARPT experiments on the liquid–solid riser, a total of 24 NaI(Tl) scintillation detectors were positioned around the riser column (Figure 3b). Figures 3b and c show a schematic diagram of the configuration, consisting of 24 detectors with two detectors at each level. The zone of interrogation of the detectors was 180 cm long. Two detectors each were fixed 12.5 cm below the datum level and 12.5 cm above the 180-cm level. The photon counts recorded by these "sentry" detectors were not used for the position reconstruction, but were used for determining the time of entry and exit of the tracer particle in the zone of interrogation. The detectors were positioned perpendicular to the riser column, and the outer discs of the detector were set at 9.13 cm from the column center. The detector crystal centers were 11.7 cm from the column center. These radial positions were determined by successive trials, such that the detectors recorded slightly less than saturation photon counts when the tracer particle was very close to the column wall. This ensured that the detectors never became saturated, and the full "range" of the crystals was also used optimally.

The calibration was performed by placing the tracer particle at numerous locations in the column, operated under the actual experimental conditions. Photon counts recorded at the detector are a function not only of the distance between the tracer (radioactive source) and the detector, but also of the density of the intervening medium. Thus, *in situ* calibration is necessary to ensure that the mean volume fraction distribution in the system is the same during calibration as it is during the actual experimental conditions. This poses practical limitations, however, and a method for positioning the tracer particle in known locations while the system is under operation became necessary. For this purpose, a calibration device (Figure 3d) was constructed, and could be introduced into the riser from the top while it was in operation. The device consisted of a metal structure lowered from a thin, rigid aluminum plate, held horizontally, and firmly bolted to the top of the riser. A circular aluminum disc, centered and mounted on this plate, served as an azimuthal scale, whereas a extended line of graduated steel segments (Figure 3d) was used to provide axial access into the column. The tracer particle was rigidly held at the tip of this arrangement and its exact location was established with the graduations on the segments and on the azimuthal scale on the top. Spring-loaded studs that pressed against the column wall locked the tracer particle in place and prevented random motion in the cross-direction.

The calibration device thus constructed could be used to rapidly position the tracer particle at many known locations. For these experiments, the tracer particle was positioned at as many as 55 tracer locations per plane, with 30 planes (that is, a total of 1650 tracer positions). For each of these positions, the

photon counts were recorded at each of the detectors at each operating condition during the calibration phase. During the actual experimental run, the tracer particle (designed to be similar to the particles constituting the solids phase) was allowed to run free in the riser and the calibration functions were used to reconstruct its position as a function of time, following the procedures outlined by Devanathan (1991) and Degaleesan (1997).

Before running the actual experiment, it was necessary to ascertain that the calibration data is satisfactory and the position of a stationary particle can be reconstructed with fidelity. This was done by choosing 50 random stationary points in the column and then reconstructing their position using the calibration data set. The maximum average error in tracer position reconstruction found at any flow condition was 3.1 $\pm$ 1.2 mm. Errors in location of the tracer particle are not uniformly distributed across the column and have a spatial variation because of the number of detectors, their relative positioning, and properties of the system. This could yield higher than average error in certain regions of the zone of interrogation of the detector and lower than average at others. In view of this, a Monte Carlo model (Larachi et al., 1994) was used to analyze spatial error (resolution and sensitivity) distribution for CARPT implementation in any setup (Roy et al., 2002). For the liquid–solid riser setup, the theoretical spatial error distribution is shown in Figure 4. Figure 4a shows the resolution in the experiments under typical conditions of flow, or the theoretically calculated error in reconstructing tracer particle position. Figure 4b shows the sensitivity of the experiment. Details of these theoretical calculations are discussed elsewhere (Roy, 2000; Roy et al., 2002). The simulated column average resolution (error in reconstruction) from the contour plot shown in Figure 4a is 2.42 $\pm$ 0.43 mm, with a maximum value (extreme top and bottom) of 3.65 mm and a minimum value of 0.86 mm. This was in good agreement with the experimentally measured values (maximum measured was 3.1 $\pm$ 1.2 mm). Note that the actual CARPT experiment (zone of interrogation) results are interpreted in the central 180 cm in the column (Figure 4), where the theoretical resolution is much better than 2.5 mm.

Results and Discussion

For the current experiments, the objective was to obtain at least 15–20% overall solids holdup in the system, which is expected to be typical solids loading desired in proposed reactors of this type.[1] The solids and liquid flow rates had to be chosen such that these conditions could be achieved in the present setup. The choice of liquid flow rate was dictated by the system design (Figure 1) and the pump characteristics. The empirical equations of Kopko et al. (1975) were used to estimate the solids-to-liquid (S/L) flow ratios that would be needed to achieve average solids holdup in the range of 20–40%. Subsequently, the eductor calibration was experimentally established (Roy et al., 2001a) and the eductor liquid flow required for delivering the desired solids flow rate was calculated.

The results of such a calculation, within the range of the operating variables that were achievable with the current setup,

---

[1] Personal communication from an interested industrial sponsor of CREL (Chemical Reaction Engineering Laboratory).
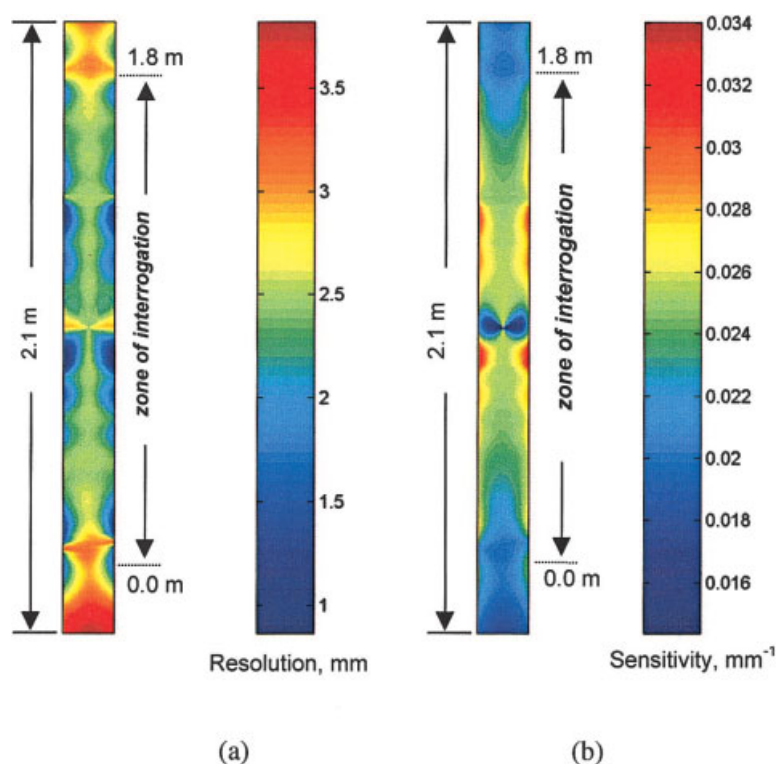
Figure 4. Theoretical distribution of (a) resolution and (b) sensitivity of the CARPT experiment in the current setup for liquid–solid riser.

[Color figure can be viewed in the online issue, which is available at www.interscience.wiley.com.]

are summarized in Table 1. Three liquid superficial velocities (0.15, 0.20, and 0.23 m/s) are used and three solid-to-liquid flow ratios (0.10, 0.15, and 0.20) are chosen at each liquid flow rate. The solids holdup in the riser was expected to be between 20 and 30% under these conditions, and this claim was checked *post facto* from the CT measurements.

Tomography measurements

Before scanning the test column under the operating conditions of interest, some "blank" scans were performed to reconstruct known distributions. For example, the riser column shown in Figure 2 was filled with water and the CT image was reconstructed to ensure that the reconstructed mass attenuation coefficient distribution was spatially uniform and close (<3.5% discrepancy) to the commonly reported theoretical
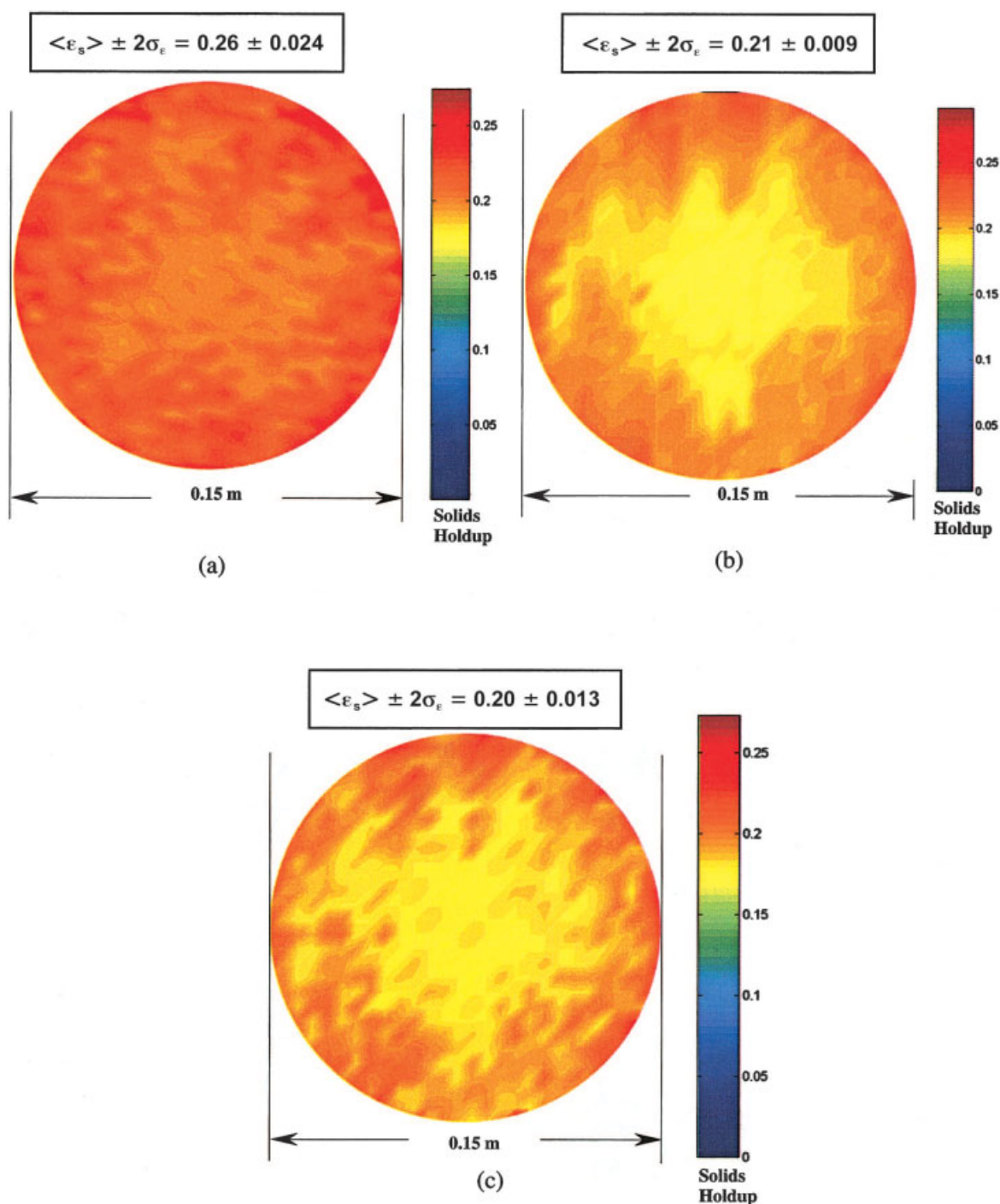
value of 0.086 cm^{-1} (Tsoulfanidis, 1983), for 660 keV gamma-ray photons (660 keV being the energy peak for Cs-137). For all image reconstruction discussed below, the actual experimental value for mass attenuation coefficient obtained in *this* setup is used.

Figure 5 shows typical scans at three different liquid superficial velocities of 0.15, 0.20, and 0.23 m/s, respectively, in which the S/L flow ratio has been maintained constant at 0.15. Qualitatively, there seems to be some minor solids accumulation at the walls. The distributions are approximately axisymmetric (note the high resolution of the contour scale). Also, there is a reduction in overall solids volume fraction with increased liquid superficial velocity. Similar scans were obtained by varying the S/L flow ratio at a constant liquid flow rate. The overall solids fraction was found to increase with the increase in the S/L flow ratio because more solids are fed into the riser section for the same overall liquid flow (and thus energy input) to the system.

These qualitative findings were quantitatively verified by making an assumption of axisymmetry and circumferentially averaging the solids volume fraction distributions. Such a plot is shown in Figure 6 for a liquid superficial velocity of 0.23 m/s and the three S/L ratios (solids volume fraction profiles are plotted at various levels in the riser). Profiles at other flow conditions are reported by Roy (2000). The error bars represent the standard deviation of the azimuthal variation of solids holdup. From the graphs, there seems to be no significant axial gradient in the solids holdup among the levels at which the scans were performed, even though the level of 0.5 m does

Table 1. Operating Conditions

| Liquid Superficial Velocity (m/s)	Total Liquid Flow Rate, $\times 10^{-3}$ (m^3/s) (eductor line + riser line)	Solids to Liquid Flow Ratio (S/L)	Estimated Solids Holdup (Kopko et al., 1975)
0.15	2.76	0.10	0.32
0.15	2.76	0.15	0.35
0.15	2.76	0.20	0.37
0.20	3.66	0.10	0.27
0.20	3.66	0.15	0.30
0.20	3.66	0.20	0.33
0.23	4.16	0.10	0.24
0.23	4.16	0.15	0.28
0.23	4.16	0.20	0.31

Figure 5. Scans at three different liquid superficial velocities.

(a) 0.15 m/s; (b) 0.20 m/s; (c) 0.23 m/s. The solids-to-liquid flow ratio was fixed at 0.15. All scans are at 1 m from the lower flange of the riser. [Color figure can be viewed in the online issue, which is available at www.interscience.wiley.com.]

seem to show marginally greater solids volume fraction compared to that of the other two levels. In the zone of developed flow in the riser, there is a visible radial gradient in solids holdup, although one cannot really identify distinct core and annular regions. The radial solids segregation is not as significant as observed in gas–solid risers (for example, Fan and Zhu, 1998). As a matter of fact, the radial solids holdup is relatively uniform, with the variation not exceeding ±25% of the mean

[compared to as much as 90% variation from the mean near the walls of a gas–solids riser (Fan and Zhu, 1998)].

Increasing the liquid superficial velocity decreases the overall solids holdup. Increasing the liquid superficial velocity (that is, increasing the overall liquid flow rate) increases the energy input to the system. Because the liquid is the only source of energy that drives the solids circulation, the solids circulation rate (and, equivalently, the solids mass flux in the riser) in-
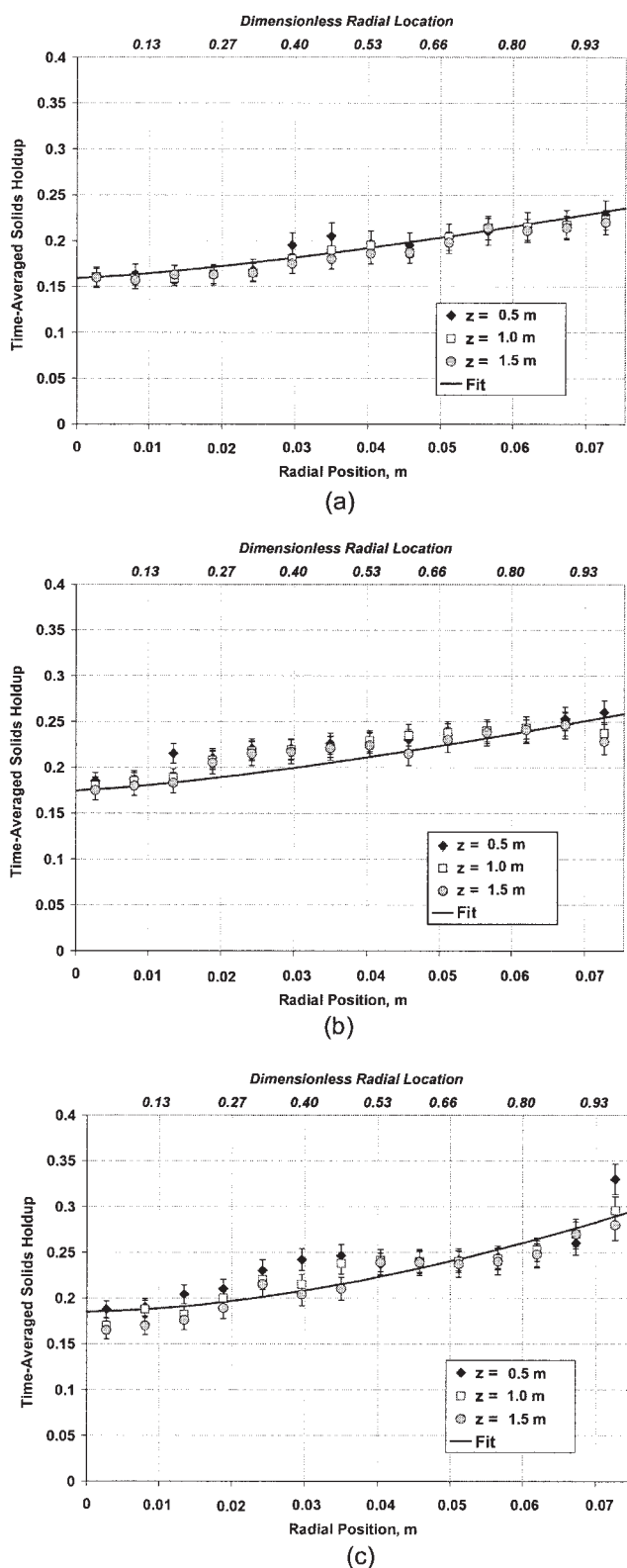
Figure 6. Circumferentially averaged time-averaged solids holdup distribution in the liquid solid riser at $U_l = 0.23$ m/s.

(a) S/L = 0.10; (b) S/L = 0.15; (c) S/L = 0.20 (bars show standard deviation of azimuthal variation).

creases in a circulating system in which the solids flux is not independently controlled. However, if the solids flow rate is determined independent of the liquid flow rate (as has been done in these experiments), then the higher liquid flow drives more solids out of the riser section into the hopper (or any other unit external to the riser). Consequently, the holdup of solids in the riser decreases. On the other hand, with an increase in solids flow rate at a fixed liquid flow, more solids are fed into the riser section so that the system achieves a new steady-state circulation pattern with more solids holdup in the riser.

It should be noted that the results, so far, do not reveal any information about the transient distribution of solids volume fraction and present only the time-averaged distribution. The exact nature of the velocity field of the solids will be discerned through the CARPT experiments presented later. From the tomography results alone, it seems that even though the solids particles may be transported in all directions in three-dimensional space inside the riser, because of the fluctuating liquid velocity field, the solid phase migrates to the periphery of the riser in a time-averaged sense. Radial migration of solids in riser flows is a complex phenomenon and is not yet properly understood (Fan and Zhu, 1998). However, solids tend to aggregate in regions in which the local slip velocity between the solids and the continuous phase is low, such as near the walls of the riser. This hypothesis should also imply that the "severity" of the segregation (that is, nonuniformity in the solids volume fraction distribution) would vary as some function of the density difference between the phases, given that the slip velocity is also directly related to the density difference. In gas–solid risers, the density difference between the solid and gas phases is very significant (three orders of magnitude) so that the radial solids segregation is severe as well. In liquid–solid systems, the densities of the two phases involved are comparable so that the solids segregation should not be very severe and the bed expansion should be relatively uniform through all the different operating conditions. These conclusions are also consistent with the results of Limtrakul (1996), who performed CT experiments in liquid–solid (batch) fluidized beds.

It is instructive to "cross-check" the CT results by comparing the overall solids volume fraction with some alternative independent measurements. Unfortunately, unlike batch systems in which the overall bed expansion may be measured, in "flow-through" systems such as the liquid–solid riser such experiments would be meaningless as indicators or overall holdup. Thus an alternative approximate measurement was adopted. At the end of each run the liquid valves were shut off very rapidly to "freeze" the overall holdup in the riser. As the liquid flow was stopped by rapid valve shutoff, the solids residing *in* the riser at the time of shutoff settled and made up a liquid-filled packed bed at the bottom of the riser. The dimensions of this bed were measured, and using for a packed bed solids volume fraction of 0.6 (based on scans made in the riser itself; Roy, 2000), a total volume of solids was estimated. This corresponds approximately to the total amount (volume) of solids in the riser section at the time of shutoff. Reported as a fraction of the total riser volume, this represents the total volume fraction (holdup) of solids in the riser under steady-state operating conditions, assuming that steady-state conditions existed at the time of shutoff. If a fully developed time-averaged profile of solids volume fraction could be assumed in the riser, then total

Table 2. Overall Solids Holdup in the Riser

Liquid Superficial Velocity (m/s)	Solids–Liquid (S/L) Flow Ratio	Cross-Sectionally Averaged Holdup Determined by CT	Holdup Measured at the End of Run (ε_{s_T})	Discrepancy (%) $\dfrac{\varepsilon_2 - \varepsilon_{s_T}}{\varepsilon_s} \times 100$	Var(ε_s) (Eq. 3)
0.15	0.10	0.24	0.25	−4.1	0.74
	0.15	0.26	0.26	0.0	0.72
	0.20	0.29	0.27	+6.9	0.71
0.20	0.10	0.19	0.20	−5.2	0.69
	0.15	0.21	0.20	0.0	0.65
	0.20	0.23	0.21	+8.6	0.62
0.23	0.10	0.19	0.20	−5.2	0.69
	0.15	0.20	0.20	+0.0	0.63
	0.20	0.22	0.20	+9.1	0.58

solids holdup calculated in this fashion can be compared to the values obtained by CT. These comparisons are listed in Table 2. Naturally, this method is at best approximate, first because the exact conditions and protocol of valve shutoff could not be standardized (because they were all manual valves meant for handling large flow rates). Second, solids tend to pack in different ways in packed beds based on conditions under which the packed beds consolidate, and the mean solids holdup in them may have a small variation.[2] The results agree within 10% at all flow conditions; for most conditions the agreement is much better.

From the available data and the conditions studied, it is clear from Table 2 that the cross-sectional average solids holdup shows a trend both with liquid superficial velocity and S/L ratio. It is also interesting to observe the character of the normalized spatial dimensionless variance of solids holdup, defined as

$$\mathrm{Var}(\varepsilon_s) = \frac{2\pi \int_0^R r(\varepsilon_s - \langle \varepsilon_s \rangle)^2 dr}{\pi R^2 \langle \varepsilon_s \rangle^2} \qquad (2)$$

Var(ε_s), defined as above, has a value of 0.0 if the solids distribution is uniform. The higher the degree of nonuniformity in the solids distribution (more radial segregation), the higher the value of Var(ε_s). Clearly, the spatial distribution of solids, normalized by the cross-sectional average at any condition, becomes more uniform with increased solids input to the riser at any given liquid flow rate. When the liquid flow is increased, the cross-sectional mean solids holdup is decreased and the time-averaged solids distribution also becomes more uniform.

Solids velocity field

Having established the information regarding the solids volume fraction profiles, the remaining results presented in this work were obtained by the use of CARPT. During a typical CARPT experiment, the tracer particle (designed to be "similar" to the particles that constitute the solids phase) is allowed to wander freely in the system and its position time series can be reconstructed from the photon counts time series recorded at each of the detectors. Figure 7a shows the typical trace of the tracer particle during a single trajectory. As the tracer particle moves around in the circulating fluidized bed loop, it periodically passes through the zone of interrogation of the detectors in the riser (Figure 3a). In each pass through the riser, completely independent trajectories are followed. Figure 7a represents one such trajectory that spanned over 38 s, generating a trace of 1900 consecutive positions (data acquired at a sampling frequency of 50 Hz). Figure 7a(i) shows the projection on the horizontal (x–y) plane, whereas Figures 7a(ii) and 7a(iii) are projections on the x–z and y–z planes, respectively. The particle takes a tortuous path, accelerating sometimes and decelerating at others, indicated by the fact that the separation between successive locations (at constant time intervals) is not constant.

In multiple passes, the tracer particle visits all positions in the column and thus traces out the fate of the solids phase as a whole as it flows through the system. Figure 7b shows the same position data (as in Figure 7a) as a function of time. Visual inspection of the position time series seems to indicate that the motion of the solids in the horizontal plane [radial coordinate, Figure 7b(i)] is principally random (dispersive) without any preferred direction. In the axial direction [Figure 7b(ii)], the motion seems to be directed upward, even though the tracer particle does flow down and then up again even during the short span of 38 s. Note that the fine-scale fluctuations [as seen in Figure 7b(i)] are also present in Figure 7b(ii), even though they are superimposed on a large-scale motion and are thus not apparent [the scale of the ordinate in Figure 7b(ii) is two orders of magnitude higher than that in Figure 7b(ii)]. Clearly, this kind of large-scale directed motion (Figure 7b) and the fine-scale random motion contribute to backmixing in the solid phase, a topic that will be discussed in greater detail later in this paper.

A time derivative of the tracer particle position estimates yields the instantaneous Lagrangian velocity time series. To make comparative studies about the behavior of the ensemble of solid particles as a whole, it is important to convert the velocity trace of *one particle* (tracer) to the time-averaged Eulerian velocity field that is representative of the *entire ensemble of particles*. To permit this calculation, a "fine-enough" imaginary grid in the three-dimensional space was assumed to make up the column, with the following segments: $\Delta r = 0.93$ cm, $\Delta z = 5$ cm, and $\Delta\theta$ varied so that the average cell volume was 32.26 cm^3. Thus in general, the azimuthal segment was varied as a function of the radial location of the control volume. The system volume was 32,148 cm^3, so that each cell or control volume was about 0.1% of the total volume.

For any two successive locations of the tracer particle, the

---

[2] Cumberland and Crawford (1987) report, for example, a series of 116 experiments of packing 0.211- and 0.25-in. solid spheres in a packed bed, in which the mean voidage of the resulting packed bed was found to vary over 0.391 ± 0.016.
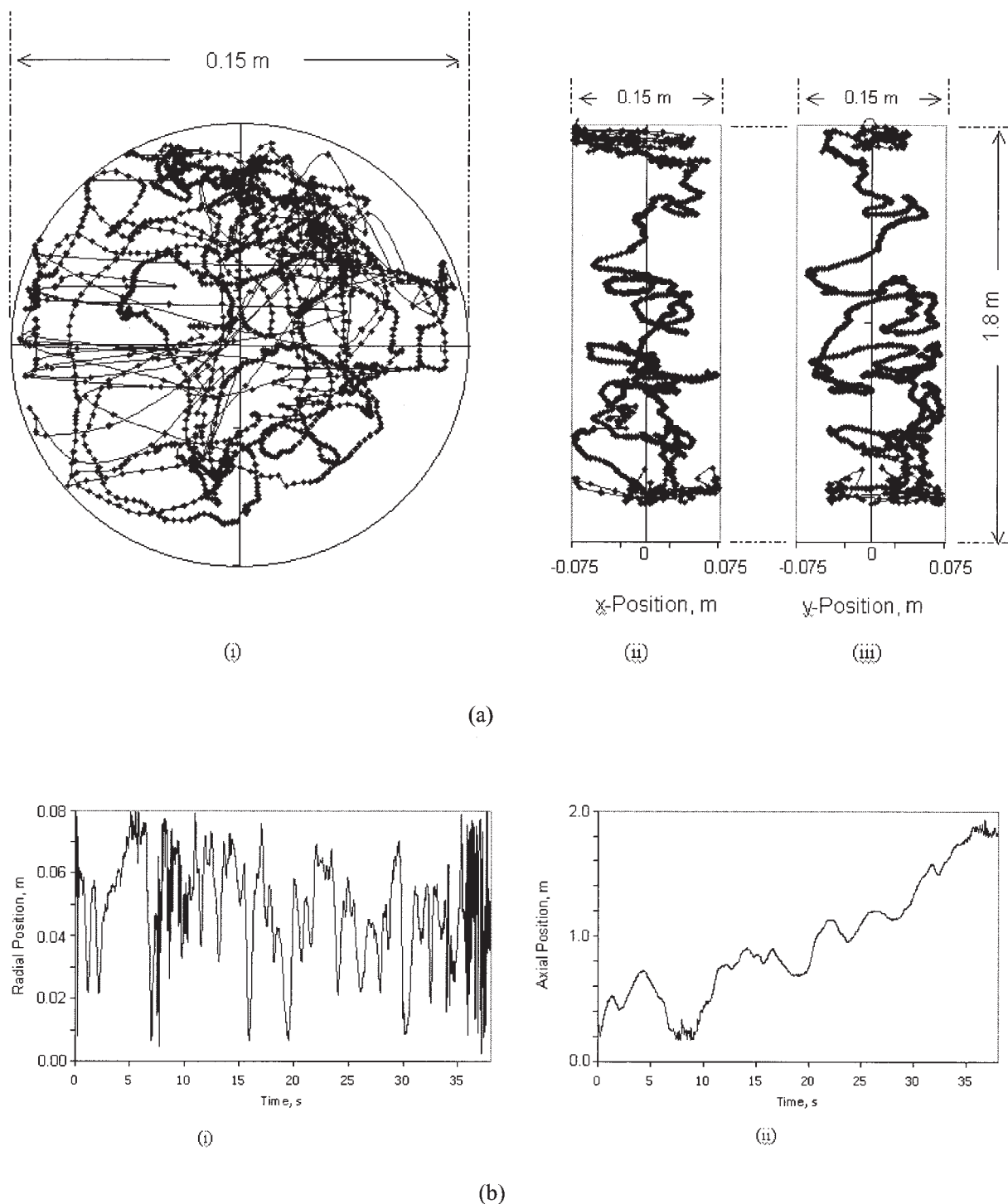
Figure 7. (a) Single trajectory of tracer particle (U_l = 0.20 m/s; S/L = 0.15) during a residence time of 38 s (1900 successive positions) in the column: (i) x–y plane; (ii) x–z plane; (iii) y–z plane; (b) typical 38-s histories of the tracer particle motion: (i) radial coordinate; (ii) axial coordinate.

velocity was calculated by time-differencing and ascribed to the cell or control volume of the grid, wherever the midpoint of this velocity vector falls. Thus, one acquires a probability density distribution (p.d.f.) of instantaneous velocities in each compartment of the grid. Consider Figure 8, in which the histogram of instantaneous velocity of the tracer particle at three radial locations (compartments) at the 0.5 m axial level, each at a $\theta = 0°$ reference location, is displayed, the operating conditions data for which are U_l = 0.23 m/s, S/L = 0.10 (the cell index *nr* increases radially outward). The histograms were constructed by monitoring the entire Lagrangian trace of the tracer particle (through all
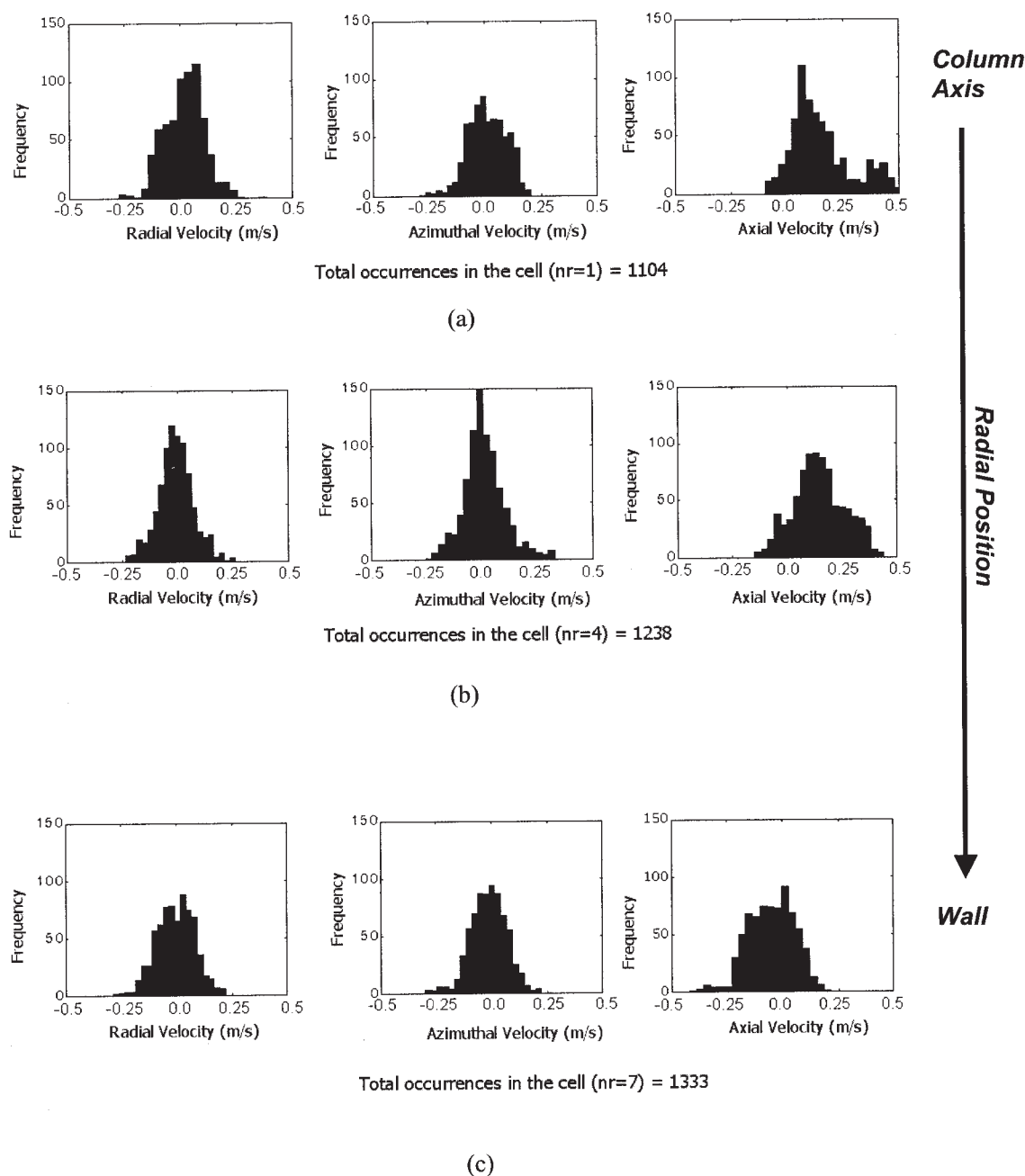
Figure 8. Probability density functions for instantaneous r-, θ-, and z-velocities at three radial locations at 0.50 m height in the riser.

nr signifies the radial compartment used in the CARPT experiment with $nr = 1$ being the column axis ($U_l = 0.23$ m/s, S/L = 0.10).

the independent trajectories), noting the instantaneous particle velocity whenever the particle passes through the compartments of choice, and inventorying the results to a file. The probability density function (histogram) of these velocity components have a well-defined mean that is close to zero for the radial and azimuthal components and a finite positive or negative value for the axial component, depending on the radial location. Invoking ergodicity (see, for example, Feller, 1968), one asserts that if we observe the trace at all points *long enough* (that is, we collect *sufficient statistics*), then the p.d.f. (like those plotted in Figure 8) *is the same as* the one we

could possibly observe (but cannot, because of practical limitations) by putting a probe at a point of interest (or a cell or compartment). The moments calculated from the ensemble of observations are thus those that could be obtained by analysis of a time series obtained at the given point. Further, we can show experimentally, post facto, that the CARPT experiments indeed reflect stationarity in the system, and quantities calculated from the raw (filtered) data indeed converge beyond a certain time window.

Once the local velocity p.d.f. values are established, the local ensemble-averaged solids velocity, as well the fluctuating com-

**Table 3. Summary of Formulas Used in CARPT Experiments**

Instantaneous radial velocity

$$v_r = \frac{2}{\Delta t}[r_2\cos(\theta_2 - \theta_1) - r_1]$$

Instantaneous azimuthal velocity

$$v_\theta = \frac{2}{\Delta t}[r_2\sin(\theta_2 - \theta_1)]$$

$$r = \frac{1}{2}\sqrt{r_1^2 + r_2^2 + 2r_1 r_2\cos(\theta_1 - \theta_2)}$$

Instantaneous axial velocity

$$v_z = \frac{\Delta z}{\Delta t}$$

Ensemble averaged velocity

$$\langle v_q(i, j, k)\rangle = \frac{1}{N(i, j, k)}\sum_{n=1}^{N(i,j,k)} v_{q,n}(i, j, k) \qquad q = r, \theta, z$$

Fluctuating velocity component

$$v_q'(i, j, k) = v_q(i, j, k) - \langle v_q(i, j, k)\rangle$$

Azimuthally averaged velocity component

$$\langle v_q(i, k)\rangle^{az} = \frac{\sum_{j=1}^{T_{\dim(i)}} \langle v_q(i, j, k)\rangle N(i, j, k)}{\sum_{j=1}^{T_{\dim(i)}} N(i, j, k)} \qquad q = r, \theta, z$$

RMS velocity

$$\langle v_q\rangle^{RMS} = \sqrt{\langle v_q'^2\rangle} \qquad q = r, \theta, z$$

Stress

$$\tau_{qs} = \rho_p \langle v_q'(i, j, k) v_s'(i, j, k)\rangle$$

Fluctuating kinetic energy per unit volume

$$KE = \frac{1}{2}\rho_p[\langle v_r'^2\rangle + \langle v_\theta'^2\rangle + \langle v_z'^2\rangle]$$

Lagrangian autocorrelation coefficient

$$R_{ij}(\tau) = \frac{\langle v_i'(t)v_j'(t + \tau)\rangle}{\langle v_i'(t)v_j'(t)\rangle} \qquad i, j = r, \theta, z$$

ponents, may be extracted by using the formulas listed in Table 3. This information yields the local mean velocities, as well as the stresses and the kinetic energy per unit volume from the "fluctuating" components of velocity. Thus, one obtains a three-dimensional velocity field from the CARPT data. Figure 9 shows a typical vector plot of solids velocity on the r–z plane at typical operating conditions ($U_l = 0.23$ m/s, S/L = 0.10). The vectors are plotted at three different r–z planes each separated by 45°. Clearly, the vectors point upward at the center of the column and downward at the wall. Also, visually the flow field looks axisymmetric (that is, independent of θ), indicating that the radial components of velocity are small. Indeed, if one plots the velocity field in the r–θ plane, one obtains a near-zero field (Roy, 2000). In Figure 9d, the flow field is azimuthally averaged and the azimuthally averaged solids velocity vectors are plotted. Even though the solid-phase particles (represented by the tracer particle) take tortuous paths in their sojourn from the inlet to the exit of the riser (Figure 7), the time-averaged picture (constructed with data collected over 40 h) is ordered with a clear pattern (Figure 9).

Before we present the effect of operating conditions on the azimuthally averaged solids velocity field, it is important to ensure that the results are statistically meaningful (that is, sufficient statistics has been collected), so that the radial profile of solids axial velocity obtained from the CARPT experiment is indeed representative of the solids flow field at a given operating condition. Figure 10 shows a typical case of time-averaged axial solids velocity profile under a superficial liquid velocity of 0.15 m/s and S/L ratio of 0.10. The velocity profiles are plotted at 0.5 m above the solids inlet plane of the riser. In Figure 10a, the entire set of data collected for the given condition ($U_l = 0.15$ m/s; S/L = 0.10), consisting of 1473 independent trajectories of the tracer particle, was used to reconstruct the radial velocity profile at a height of 0.50 m above the solids inlet plane in the riser. Subsequently, three quarters of the data set (1104 trajectories, chosen randomly

from the entire data set) and half the data set (740 trajectories, also chosen randomly) were used to reconstruct the velocity profiles. It is apparent that with 1104 or more trajectories, the reconstructed velocity profile of the solid phase is convergent and does not vary with increasing length of the experiment. With only 740 trajectories, however, there are some small deviations in the calculated velocity profile, when compared with the calculation based on the entire data set. This "convergence" of velocity profiles corresponds to collection of *sufficient statistics*, so that the (normalized) probability density functions plotted in Figure 8, for example, do not change with further increase in the number of occurrences. This reflects *reproducibility* of the CARPT experiments because each trajectory is independent and can be chosen in *any* sequence from a set of runs (at any given condition) done in *any* order. In Figure 10b, the adopted grid is further subdivided so as to halve the size of each radial compartment. This leads to an almost fourfold reduction in volume of each compartment and, consequently, a roughly proportional reduction in the number of tracer occurrences in *each* compartment used for ensemble averaging of the instantaneous velocities. Clearly, the velocity profile reconstructed thus is less "smooth" compared to that reconstructed using the relatively coarser grid (with a volume of about 32 cm³ per cell, with each cell being about 0.1% of the total system volume), even though both profiles are approximately the same. The message from the two figures in Figure 10 is that one has to choose an optimal grid size, optimum length of experiment (determined by the frequency of data acquisition and volume of vessel), and occurrences per compartment required for convergence to the final result.

Figure 11 shows typical time-averaged azimuthally averaged axial solids velocity profiles. The data in Figure 11 are at 0.23 m/s, at S/L ratios of 0.10, 0.15, and 0.20, respectively, and at three levels (0.5 m, 1.0 m, and 1.5 m) in the column at each condition (error bars show the azimuthal variation at each level). Profiles at other liquid velocities have been reported by
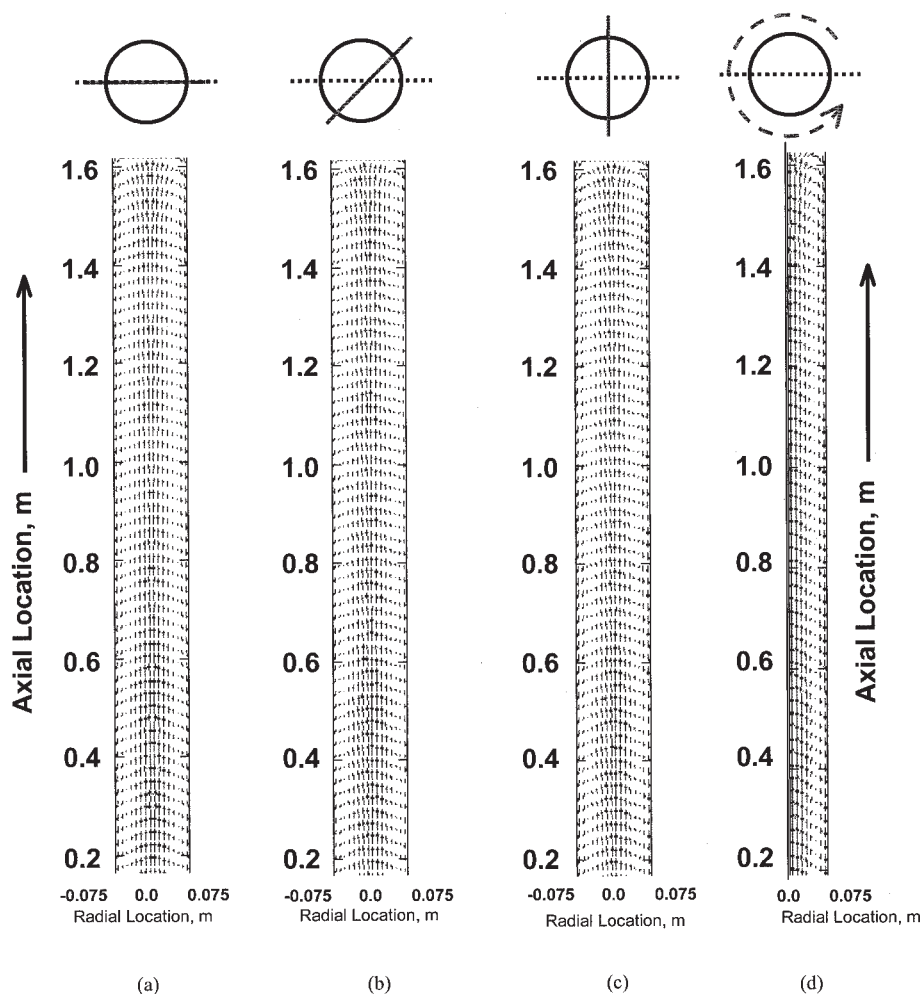
**Figure 9. Solids velocity vector plots at U_l = 0.23 m/s, S/L = 0.10.**

(a) In a typical *r–z* plane. (b) At 45 ° to first plane. (c) At 90 ° to first plane. (d) Flow field has been azimuthally averaged (0–360°) to yield an axisymmetric velocity vector plot. (Vectors have been interpolated between planes to yield a more uniform vector plot. Longest vector represents a velocity of 0.20 m/s.)

Roy (2000). In all such profiles, one observes that the solids flow above 0.50 m is fully developed in the time-averaged sense, and no significant variation in the radial profile of the axial component of solids velocity is observable. The "devel-opedness" of the flow field should be viewed in the broader perspective of the flow being stationary. There are clearly variations in the instantaneous velocity both along the axial location as well as in the cross-sectional plane (Figure 7), but the timescales associated with these variations are much smaller when compared to the time window in which the data are averaged. Although the local variations can *never* be re-produced by any number of experiments, the time-averaged developed velocity profile is reproducible and statistically sig-nificant.

One also notes that at all conditions (Figure 11), there is an annulus of solids at the wall that is flowing down in a time-averaged sense. The solids velocity is roughly parabolic, the highest velocity being at the center of the column, and negative near the wall. The exact location of the "cross-over" (that is, the location at which the profile crosses the abscissa) does not appear to show any trend. In fact, within the spatial resolution of the

velocity reconstruction, in almost all the cases the cross-over point corresponds to the same compartment (Figure 11). The downflow of solids at the wall is expected to cause considerable backmixing in the solid phase. Because the solids holdup is higher at the wall, compared to the center of the column (Figure 7), the annulus of negative velocities at the wall makes for significant mass flow of solids downward in the column. A more quantitative estimate of this downflow follows.

At a fixed liquid superficial velocity, an increase in the S/L flow ratio increases the solids velocity (Figure 11). At a higher S/L flow ratio into the system solids holdup in the riser section is larger for the same overall liquid superficial velocity. This increases the interstitial velocity of the liquid phase, and thus the velocity of the solid phase, which draws energy from the former. However, the increase in solids velocity is not linearly proportional to the increase in liquid superficial velocity. Be-cause of the increased solids holdup and thus the increased probability of collisions between solid particles (and solid particles and wall), there is an increase in momentum loss arising from solid–solid interactions (and solid–wall interac-tions). These two effects offset each other and lead to an
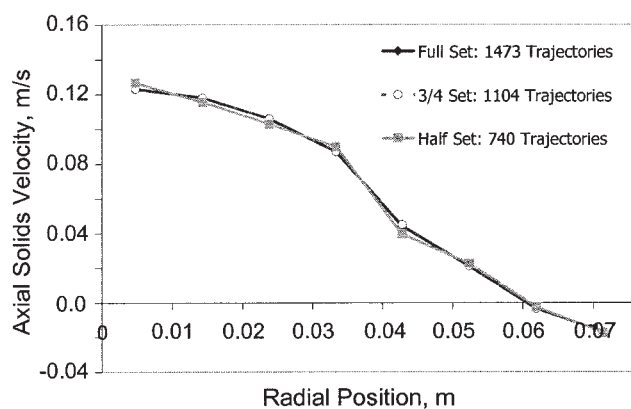
(a)
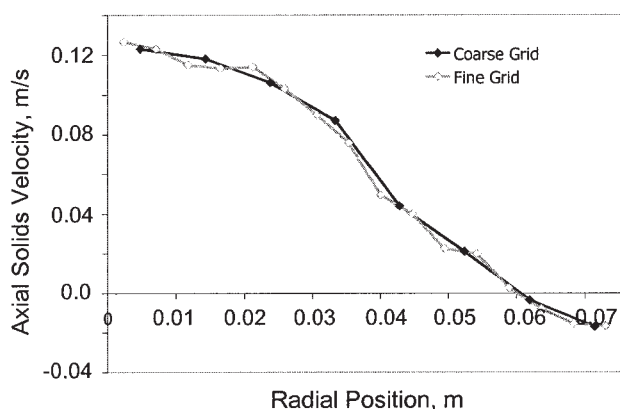
(b)

Figure 10. Typical azimuthally averaged time-averaged solids velocity profile, illustrating the effect of statistics of ensemble averaging (U_l = 0.15 m/s; S/L = 0.10).

(a) Results obtained by using different quantities of experimental data. (b) Effect of grid size on radial velocity profile.

intermediate value of solids velocity in the riser stemming from an increase in solids flow rate at a fixed liquid superficial velocity. At higher liquid superficial velocities, the absolute magnitude of solids holdup (at any of the S/L flow ratios) is smaller (thus fewer particle–particle collisions), and thus the increase in mean axial solids velocity is more pronounced with an increase in liquid–solid flow ratio. One must note that the change in the mass fluxes in the riser at different S/L ratios must be reflected in the change in the pressure head of the slurry exiting at the top of the riser.

### Overall continuity closure and data reconciliation

At this stage, it is instructive to use the axially averaged mean velocity of solids to check the overall mass balance (continuity) of the solids in the riser. Note that the solids feed rate into the riser was established independent of the CARPT–CT experiments using an elaborate eductor calibration procedure (Roy, 2000; Roy et al., 2001a). Thus, we can now use those independent measurements as a benchmark and com-
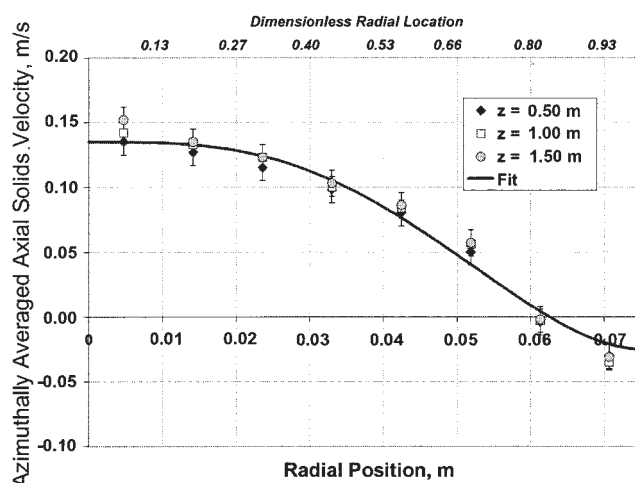
(a)
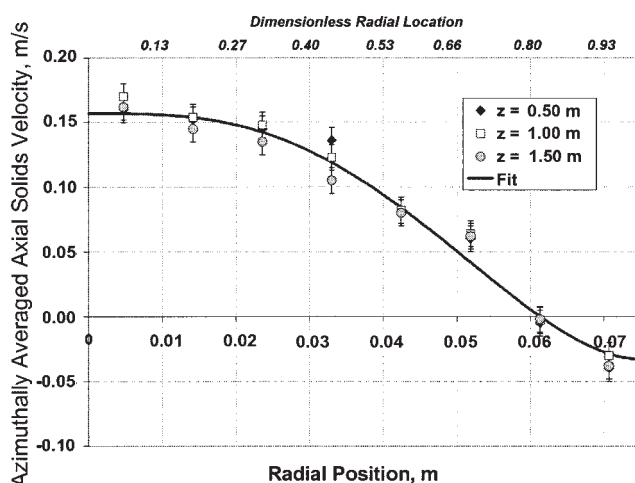
(b)
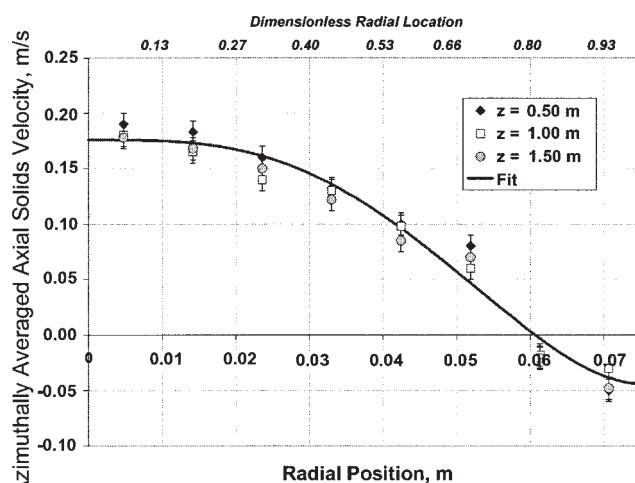
(c)

Figure 11. Azimuthally averaged time-averaged axial solids velocity profiles as a function of radial and axial position, at a liquid superficial velocity of 0.23 m/s.

(a) S/L = 0.10; (b) S/L = 0.15; (c) S/L = 0.20 (error bars represent ±2σ in azimuthal variation at any level).

Table 4. Overall Continuity Checks on the Riser

Liquid Superficial Velocity (m/s)	Actual Eductor Solids Flow Rate, $Q_{se} \times 10^{-4}$ (m³/s)	Solids Upflow Rate, $\times 10^{-4}$ (m³/s)	Solids Downflow Rate (m³/s)	Net Solids Flow Rate, $Q_{sa} \times 10^{-4}$ (m³/s)	Percentage of Solids in Downflow (%)	Discrepancy (%) $\left(\dfrac{Q_{sa} - Q_{se}}{Q_{se}}\right) \times 100$
0.15	2.78	2.78	1.89×10^{-5}	2.58	7.3	−6.8
0.15	4.16	4.29	3.12×10^{-5}	3.97	7.9	−4.5
0.15	4.54	4.80	6.31×10^{-5}	4.23	14.9	−6.9
0.20	3.66	3.53	3.16×10^{-5}	3.28	9.6	−10.3
0.20	5.49	5.55	5.68×10^{-5}	4.98	11.3	−9.1
0.20	6.50	6.88	8.83×10^{-5}	5.99	14.7	−7.8
0.23	4.23	4.86	4.42×10^{-5}	4.42	10.0	+4.5
0.23	6.38	6.50	6.94×10^{-5}	5.80	11.9	−8.9
0.23	8.01	7.51	1.07×10^{-4}	6.76	15.8	−9.3

pare against the overall solids flow rate calculated from the CARPT and CT measurements. The overall solids flow rate, upflow rate, and downflow rate are estimated, respectively, as

$$\langle Q_s \rangle \approx 2\pi \int_0^R r \langle \varepsilon(r) \rangle \langle v_z(r) \rangle dr \qquad (3a)$$

$$\langle Q_s \rangle^{up} \approx 2\pi \int_0^{R_i} r \langle \varepsilon(r) \rangle \langle v_z(r) \rangle dr \qquad (3b)$$

$$\langle Q_s \rangle^{down} \approx 2\pi \int_{R_i}^R r \langle \varepsilon(r) \rangle \langle v_z(r) \rangle dr \qquad (3c)$$

In the above equations, R_i is the radius of inversion, that is, the point at which the axial solids velocity is zero. The time-averaged velocity and solids volume fraction profiles are estimated from the CARPT and CT results, respectively.[3] Equations 3a–3c can be treated only as an *estimate* of the overall flow rate of solids, given that a term $\langle \varepsilon'(r) v_z'(r) \rangle$ involving the correlation of holdup fluctuations and velocity fluctuations has been neglected. This cross-correlation term would be zero if the entire flow is homogeneous and the time averages were exactly equal to the actual holdup and velocity distributions prevailing at all times. In the real case, the flows are vigorously fluctuating and thus the holdup-velocity cross-correlation may have a finite contribution to the overall flow rate of solids in the Eq. 3 system. Unfortunately, with CT one is able to recover only the time-averaged holdup distribution, and not the statis-

tics of the fluctuations, and thus this term cannot be estimated with acceptable accuracy. Nevertheless, we attempt to compare the predictions of Eqs. 3a–3c with the flow rate calculated from the eductor calibration (Roy, 2000; Roy et al., 2001a).

The results of such an analysis are presented in Table 5. For most conditions, the discrepancy in the overall solids flow rate estimates obtained by the two methods is within 10% (except at $U_l = 0.20$ m/s; S/L = 0.10). This is indeed a very acceptable agreement, given the fact that we are comparing data obtained by three independent experiments (CARPT, CT, and eductor

Table 5. Comparison of the Mean Velocity Measurements by Direct Calculation from Residence Times and CARPT–CT Profiles

Liquid Superficial Velocity (m/s)	Solids–Liquid Flow Ratio	Solids Velocity from LHS of Eq. (4) (m/s)	Solids Velocity from RHS of Eq. (4) (m/s)	Discrepancy (%)
0.15	0.10	0.063	0.068	−7.3
	0.15	0.077	0.084	−8.3
	0.20	0.105	0.099	+6.6
0.20	0.10	0.091	0.096	−5.2
	0.15	0.128	0.139	−7.9
	0.20	0.139	0.147	−5.4
0.23	0.10	0.113	0.129	+12.0
	0.15	0.131	0.133	−1.5
	0.20	0.149	0.142	+4.9

---

[3] To calculate the solids volumetric flow from CT and CARPT data (which are available only in discrete control volumes or pixels), it was necessary to extrapolate both the holdup and axial velocity plots to the center as well as the wall of the column. Equations 2 and 4 were used.

calibration) each of which has its own associated cluster of errors. At all the conditions studied, the solids downflow in the annulus of the riser is between 7 and 16% of the total solids flow rate. This fraction seems to increase slightly with the increasing S/L flow ratio at a fixed liquid superficial velocity, thus indicating that increasing the solids flow into the riser increases the backmixing in the solids phase. With increasing solids flow rate at a fixed liquid flow rate, the probability of particle–particle collisions is increased so that the dispersion of particles is higher (this effect is indeed observed in the measured dispersion coefficients). Consequently, axial mixing of solids is increased. In a time-averaged sense, this contributes to higher net downflow of solids. The downflow fraction also increases with increasing liquid velocity at a fixed S/L flow ratio because added energy to the system (through higher flow rate) also leads to greater turbulence (more energy dissipation) and, consequently, higher dispersion and backmixing in the solid phase.

It is noteworthy that in Table 4, the solids flow rate calculated from the CARPT and CT profiles is systematically smaller compared to that predicted by the eductor flow (except at $U_l = 0.23$ m/s, S/L = 0.10). A possible explanation of this systematic discrepancy could lie in the unknown contribution of the velocity–holdup cross-correlation term in Eq. 3, which has been neglected. Also, visual inspection of the riser during continuous operation seemed to indicate some minor segregation of solids at the lower levels (where the eductor enters the riser). The solids flow rate calculation from CARPT and CT was done using the developed profiles (above this level of axial segregation) because of practical limitations, and so this effect is missed in the collected data. Unfortunately, the presence of the flanges and the eductor connection prevented conducting any CT experiments at these lower levels of the riser; thus axial holdup variation at these levels could not be experimentally captured.

The overall mass balance (continuity) constraints can also be tested in an alternative fashion. This involves the principle that the ensemble average of the average axial velocity of the tracer particle in each of its multiple sojourns in the riser should be equal to the cross-sectionally averaged time-averaged axial solids velocity calculated. Mathematically, this can be written as

$$\frac{1}{N_{traj}} \sum_{i=1}^{N_{traj}} \overline{v_{z_i}} = \frac{\int_{r=0}^{R} r \langle \varepsilon(r) \rangle \langle v_z(r) \rangle dr}{\int_{r=0}^{R} r \langle \varepsilon(r) \rangle dr} \quad (4)$$

To calculate the left-hand side of Eq. 4, the average axial velocity, $\overline{v_{z_i}}$ is estimated by dividing the distance between the inlet and exit planes of the riser by the time of residence of the tracer particle during each of its sojourns from the inlet to exit of the riser. Subsequently, the ensemble mean average axial velocity is calculated to evaluate the left-hand-side term. Note that in this calculation the "reconstructed" CARPT velocity is not used; rather only the filtered raw data are used. The right-hand side of Eq. 4 is estimated using the *reconstructed* CARPT velocity profile and CT holdup profile. Table 6 shows the comparison, indicating reasonably good agreement between the two methods. This is an indication that not only were the experiments satisfactorily conducted with respect to close mass

Table 6. Comparison of Downflow Fraction Calculations

Liquid Superficial Velocity (m/s)	Actual Eductor Solids Flow Rate, $Q_{se} \times 10^{-4}$ (gpm)	Percentage of Solids in Downflow (%)		Discrepancy (%)
		From Profiles	Direct Enumeration of Trajectories	
0.15	2.78	7.3	8.1	−9.8
	4.16	7.9	8.7	−9.2
	4.54	14.9	13.1	−13.7
0.20	3.66	9.6	10.1	−4.9
	5.49	11.3	10.9	+3.7
	6.50	14.7	13.2	+11.4
0.23	4.23	10.0	9.1	+9.9
	6.38	11.9	12.3	−3.2
	8.01	15.8	14.7	+7.5

balance, but also that the CARPT data collection and reconstruction procedures are self-consistent and confirmed by independent means.

Finally, we note that the fraction of time that the solids are flowing up (and a corresponding fraction of downflow) is a piece of information that is directly contained in the trajectories themselves. We note at any given horizontal plane in the riser, if the z-component of time-averaged solids velocity is directed positive (upward), then the tracer particle is in upflow while crossing the plane, and similarly in downflow if the velocity vector (z-component) is directed downward. If one interrogates all the trajectories at some reference horizontal planes in the riser column, then the fraction of times that the trajectories are directed upward indicates the fraction of time the solids are flowing upward, *as long as* sufficient statistics is collected. This can be directly compared against the upflow fraction calculated from the CARPT and CT profiles, as in Eqs. 3b and 3c, and is reported in Table 6. Note that such a calculation does *not* mean that *only* trajectories in the annulus of the riser point downward (and those in the core point upward). There are both up-pointing and down-pointing trajectories in both regions, but the fraction of up-pointing trajectories (and thus the probability of solids flowing up) is higher in the core, leading to net positive axial velocity.

RMS velocities and kinetic energies

To characterize the random and fluctuating behavior of a "continuum" fluid, it is conventional to study the spatial correlations (second-order moments) of the fluctuating velocity field (for example, Frisch, 1996; Tennekes and Lumley, 1972). The correlations $\langle v'_q v'_s \rangle$ (where q and s are coordinate directions) are directly related to "Reynolds' stresses," and can be thought of as capturing the role of fluctuations in the q-component of velocity in transporting momentum in the s-

direction, and vice versa. It is important to note, however, that in such a description, *all* scales of turbulence are grouped together and information about the distribution of kinetic energy of fluctuations among the individual scales is lost.

Because CARPT provides an assessment of the fluctuating velocity field as well, it is instructive to adopt a similar approach to characterize the fluctuations in the solids phase. The procedure followed is to subtract out from the fluctuating velocities the time-averaged mean velocity components, and subsequently cross-correlate the fluctuating components. The mathematical formulas are listed in Table 3 and the details of the treatment have been presented elsewhere (Degaleesan, 1997; Devanathan, 1991; Roy, 2000). We note, however, that because of limitations on the frequency of data acquisition (50 Hz), the highest frequency that can be captured with any degree of accuracy would be 25 Hz (adopting the Nyquist criterion). Thus, the fluctuations that occur at any higher frequency are not captured in these experiments and the contribution of those scales to the correlations, and thus to the kinetic energies, is not accounted for. This is a limitation of the experimental method and can be improved in principle by increasing the frequency of data acquisition.

Figure 12 is a plot of kinetic energy of fluctuations per unit volume of solids (see Table 3 for definitions). In Figure 13a, the axial root-mean-square (RMS) velocities for the solids, as a function of S/L flow ratios at a given liquid superficial velocity, are presented. Figure 13b is a similar plot for radial RMS velocities (both KE per unit volume, as well as "stress," have the same units of dynes/cm^2 or erg/cm^3). All the results have been azimuthally averaged and averaged axially in the region of developed flow in the riser. Note that the radial RMS velocities are not negligible, but are in fact of comparable magnitude to the axial components. Recall that the mean radial velocity was negligibly small and could be ignored when compared to the mean axial velocity.

Clearly, the kinetic energy (and the RMS velocities) increases substantially with an increase in the superficial velocity of the liquid. This is to be expected because, with increasing liquid superficial velocity (flow rate) of the liquid, there is more energy input to the system, and thus a larger fraction of input energy is eventually dissipated by the solids velocity fluctuations. Energy is dissipated by the liquid-phase turbulence as well, although the present CARPT experiments (in which the solid phase was traced) do not capture that effect.

Also, it is apparent that the RMS velocities and the kinetic energy per unit volume for the solid phase are reduced slightly with an increase in the S/L flow ratio at a given liquid superficial velocity. With increased solids holdup, large variations in instantaneous particle velocity are suppressed because of an increased lack of freedom of movement of individual solid particles (and the tracer particle). In other words, the average distance that the tracer particle (or any particle in the solids ensemble) travels between two successive collisions with other particles is reduced. Also, note that the energy from the liquid phase is fixed (superficial velocity and inlet pressure being fixed), yet a larger solids flow rate (at higher S/L ratio) has to be supported. This results in the mean velocity of solids (in addition to the mean holdup) being higher. Consequently, less energy is available for the dissipative fluctuating motion of the solid phase.

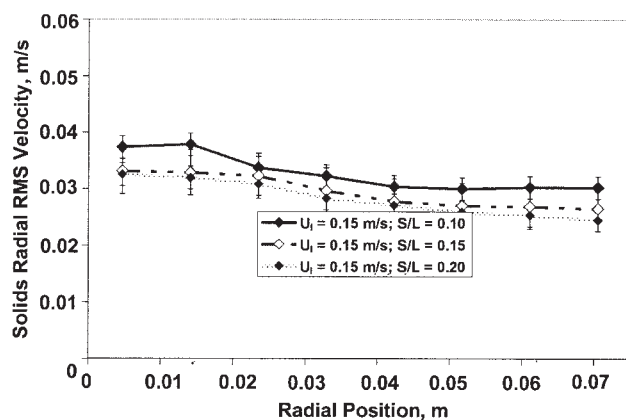The fact that the distance between successive collisions

(a)

(b)

(c)
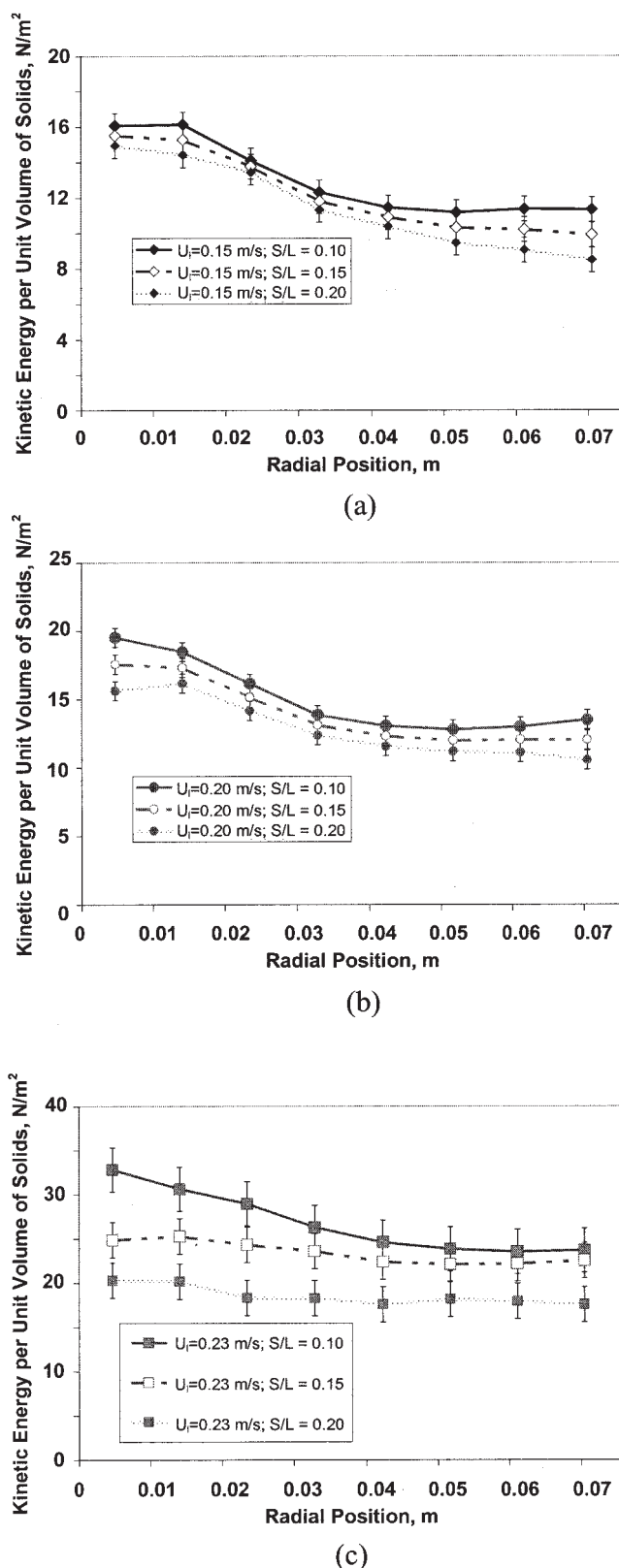
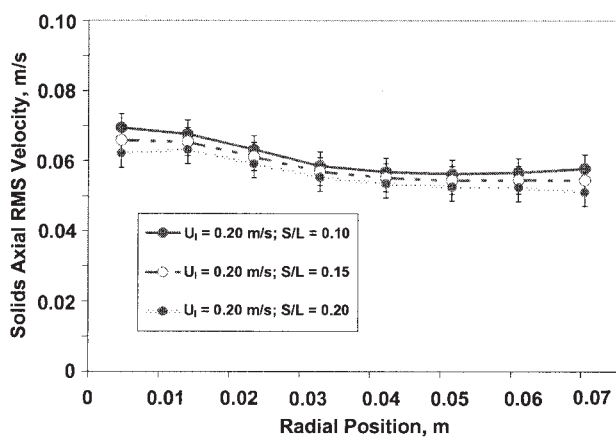**Figure 12. Fluctuating kinetic energy per unit volume of solids as a function of S/L flow ratio.**

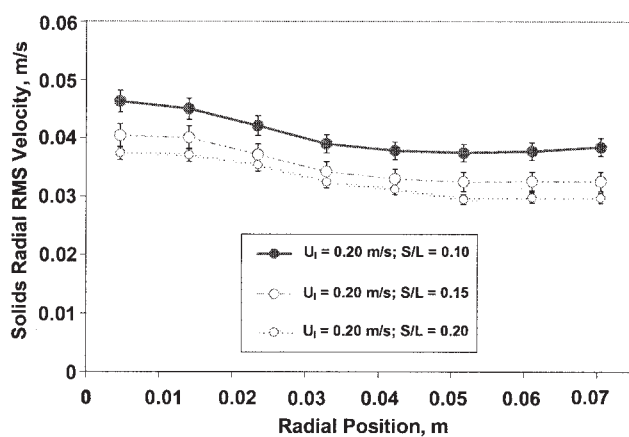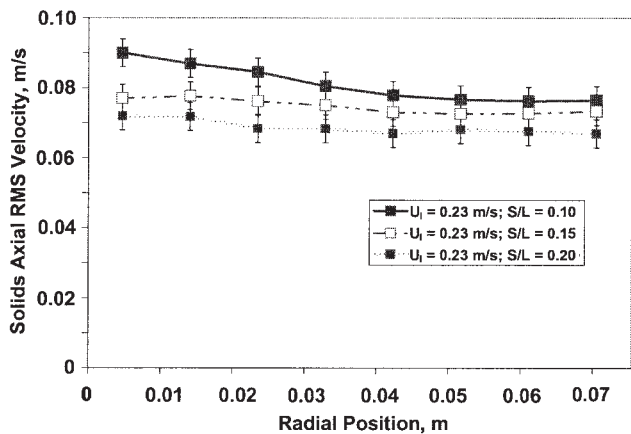(a) $U_l = 0.15$ m/s; (b) $U_l = 0.20$ m/s; (c) $U_l = 0.23$ m/s.
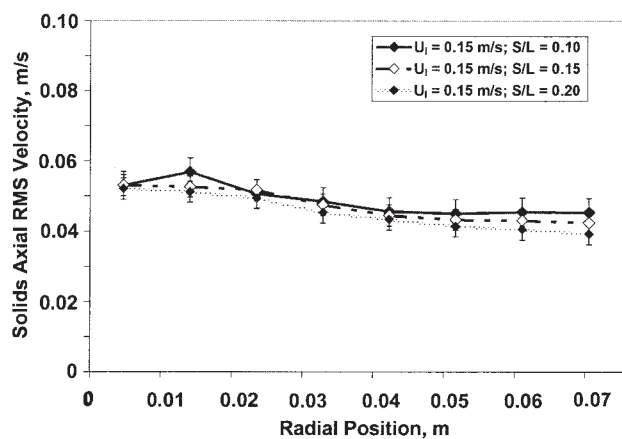
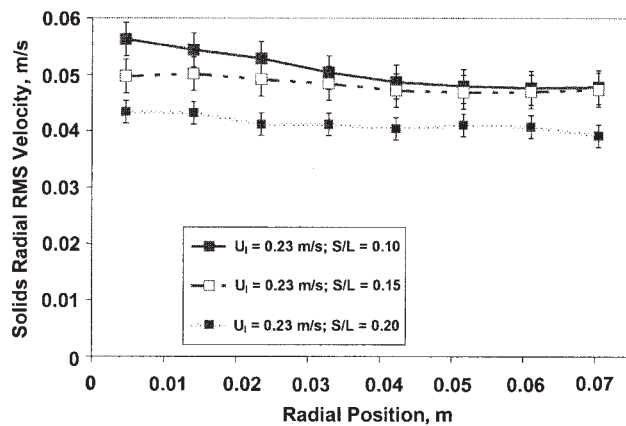Figure 13. (a) Axial RMS velocities of solids as a function of S/L flow ratio: (i) U_l = 0.15 m/s; (ii) U_l = 0.20 m/s; (iii) U_l = 0.23 m/s; (b) radial RMS velocities of solids as a function of S/L flow ratio: (i) U_l = 0.15 m/s; (ii) U_l = 0.20 m/s; (iii) U_l = 0.23 m/s.

faced by *any* particle decreases with higher solids holdup is reflected in the fact that the RMS velocities and the kinetic energy are seen to be somewhat higher at the center of the column compared to that at the walls. At any given condition, we have noted that the solids holdup is smaller at the center of the column than that at the walls. Thus, the two observations (made from independent measurements) are indeed consistent. The fact that the variation in RMS velocities and kinetic energy is not remarkable between the center and wall of the column is a result of the fact that the solids distribution variation is also not remarkable. Both liquid and solid phases have comparable inertia and thus inhomogeneities in the flow field are smaller compared to those in gas–liquid and gas–solid systems. The suppression of solids-phase fluctuations with increasing solids volume fraction is an observation also noted by Nouri et al. (1987), who performed experiments with downward solids–liquid flow in a pipe with spherical particles (100–500 μm) and solids fraction in the range of 0.1–14%.

We also note, from Figures 13a and b, that the axial RMS velocities are roughly twice those of the corresponding radial components. Similar observations were made by Devanathan (1991) and Degaleesan (1997) in gas–liquid systems (bubble columns). This indicates that the fluctuations in the solid phase generated by motion of larger-scale vortical structures as well as smaller-scale fluctuations (analogous to continuous phase "turbulence") are not isotropic and are higher in the axial direction (direction of mean flow). Thus, most of the fluctuating kinetic energy is in the z-direction, and should also contribute to higher dispersion of solids in the z-direction.

Normal and shear components of correlations

Figure 14 shows all the components of the "turbulent stress" tensor (cf. Table 3) at two typical operating conditions (U_l = 0.15 m/s, S/L = 0.10 and U_l = 0.23 m/s, S/L = 0.20). These "stresses" (that is, correlations of fluctuating components of solids velocity) arise because of solids velocity fluctuations. The behavior of the "stress" components at all other conditions is qualitatively similar.

In general, the axial normal stress is more than twice the radial and azimuthal normal stress components. The behavior of the azimuthal normal stress component (and RMS velocity) is similar to the behavior of the corresponding radial components presented in Figure 14. Both the radial and azimuthal components of the normal stress are of magnitudes comparable to the r–z component of the shear stress. The θ–z and r–θ components of stress are much lower. Note that the principal direction of solids flow is the z-direction and results in a radially outward transport of z-momentum. Thus, fluctuations in the z- and r-directions have a relatively strong correlation, resulting in the higher r–z component of the "stress." There is no net flow in the θ-direction and there the flow is approximately circularly symmetric, so that the fluctuations in the θ-direction have a much lower degree of correlation with those in the r- and z-directions. Consequently, the corresponding components of stress are much smaller.

These results, coupled with the velocity field results and solids holdup profiles presented earlier, seem to confirm that a two-dimensional axisymmetric approximation may be an appropriate framework for modeling the solids flow pattern.
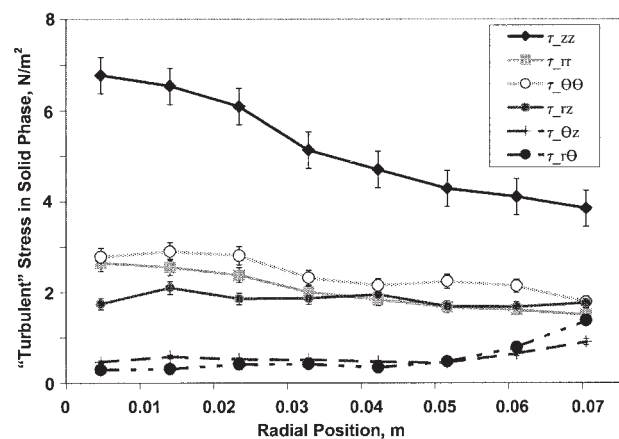
(a)
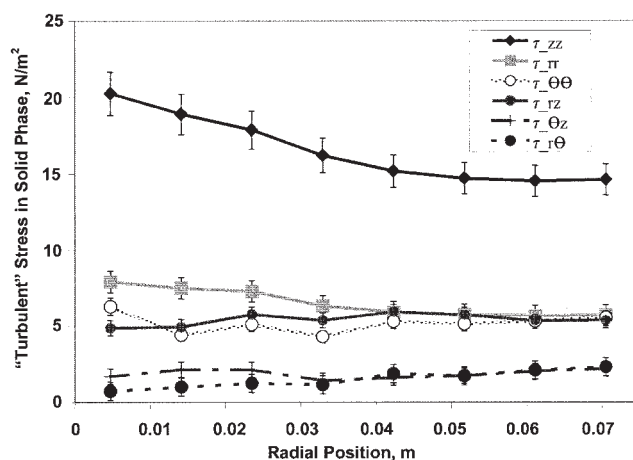
(b)

Figure 14. Components of stress tensor at some typical conditions.

(a) U_l = 0.15 m/s, S/L = 0.10; (b) U_l = 0.23 m/s, S/L = 0.20.

Kinetic energy budget

It is instructive to investigate the energy flows into the riser system and make an order-of-magnitude estimate of the various terms in the energy balance. Note that this is a multiphase flow system in which the energy input is only through the liquid phase. The incoming energy is distributed among:

- mean flow field of liquid
- mean flow field of solids
- solid-phase fluctuations, eventual dissipation by inelastic collisions
- liquid-phase turbulence and dissipation
- dissipation by friction between the phases (considering the drag between the time-averaged velocity fields of the liquid and solid phases as well as the correlation between fluctuations within the two phases)
- dissipation by wall friction in the liquid phase
- energy losses arising from (inelastic) collisions between particles and column wall
- other energy losses at entry, exit, eductor, liquid distributor, and so forth

Table 7. Energy Budget in the Riser

Liquid Superficial Velocity (m/s)	Solids–Liquid Flow Ratio	Kinetic Energy Flow Rate of Incoming Liquid (W)	Mean Kinetic Energy Flow Rate of Solids (W)	Fluctuating Kinetic Energy Flow Rate of Solids (W)	Total Energy Flow Rate of Solids (W)	Fraction of Incoming Liquid Energy in Solids Flow	Intensity of Solids Fluctuations
0.15	0.10	3.013×10^{-2}	2.685×10^{-3}	4.268×10^{-3}	6.953×10^{-3}	0.25	1.59
0.15	0.15	3.013×10^{-2}	3.440×10^{-3}	4.216×10^{-3}	7.656×10^{-3}	0.25	1.23
0.15	0.20	3.013×10^{-2}	5.246×10^{-3}	2.788×10^{-3}	8.034×10^{-3}	0.27	0.53
0.20	0.10	7.144×10^{-2}	3.753×10^{-3}	6.253×10^{-3}	1.001×10^{-2}	0.14	1.66
0.20	0.15	7.144×10^{-2}	1.199×10^{-2}	1.236×10^{-2}	2.434×10^{-2}	0.34	1.03
0.20	0.20	7.144×10^{-2}	1.5601×10^{-2}	1.060×10^{-2}	2.620×10^{-2}	0.37	0.68
0.23	0.10	1.087×10^{-1}	9.106×10^{-3}	1.948×10^{-2}	2.858×10^{-2}	0.27	2.13
0.23	0.15	1.087×10^{-1}	1.934×10^{-2}	2.134×10^{-2}	4.067×10^{-2}	0.37	1.10
0.23	0.20	1.087×10^{-1}	2.499×10^{-2}	1.999×10^{-2}	4.4984×10^{-2}	0.41	0.79

From the experiments performed as part of the present research effort, not all the modes of energy distribution and dissipation could be measured. Nevertheless, it is instructive to calculate the quantities that can be deduced from the present set of data. This serves as a check by ensuring that the measurements are physically reasonable and also generates a quantitative "estimate" for the energy flow.

Table 7 provides an assessment of the energy distribution in the incoming liquid, solids mean flow, and fluctuating solids flow field. Note that because the system involves multiple flowing phases whose volume fractions (and densities) are not the same, a fair comparison is possible only with an "integral" analysis, that is, comparing the total energy input with the incoming liquid, total energy flow rate with the mean solids flow, and the total energy flow rate in the fluctuating solids field. The intensity of fluctuations was defined—analogous to the classical definition of intensity of turbulence—as the ratio of total fluctuating kinetic energy of the solid phase to the kinetic energy of mean flow in the solid phase. This definition was adopted instead of an "intensity of turbulence" for *each* coordinate direction because the mean velocity (and thus the kinetic energy of mean flow) in the radial and azimuthal directions is close to zero.

The conclusions from Table 7 are in keeping with the earlier deductions. With increasing solids flux at any given liquid flow rate, the solid phase extracts a larger fraction of energy from the liquid phase to support the higher solids flux. (This will be reflected in a higher pressure drop across the length of the riser.) Also, at higher solids fluxes, a larger fraction of this energy is retained by the mean solids flow and a smaller fraction dissipated by solid-phase fluctuations, as indicated by the reduced "intensity of fluctuations."

Rescaled range (R/S) analysis

Thus far, all the data analysis that has been presented assumes a Eulerian perspective of the solids flow field; that is, the

frame of reference is attached to the column and the time-averaged quantities characterizing the flow are in some sense with reference to that frame, and treating the solids phase as a pseudo-continuous fluid. In what follows, the treatment is modified somewhat in that the data analysis is performed "following the tracer particle," that is, in a Lagrangian manner.

Rescaled range (*R/S*) analysis is a method of characterizing the fluctuations in the Lagrangian solids velocity field from a global perspective. *R/S* analysis is a mathematical technique aimed at determining the nature of fluctuations in any time series signal. In the particular case of particle tracking in a liquid–solid riser, where the tracer particle has been designed such that it represents any given solid particle in the system, a study of the rescaled range of the instantaneous tracer particle position and velocity reveals information about the underlying dispersion and mixing mechanisms.

If the time series of a variable $\xi(t)$ is monitored continuously, then over a timescale $n\tau$ in which the time series is recorded, the mean, standard deviation, and accumulated departure from the mean are given, respectively, by

$$\langle \xi \rangle_{n\tau} = \frac{1}{n\tau} \sum_{t=1}^{n\tau} \xi(t) \tag{5a}$$

$$S = \left[\frac{1}{n\tau} \sum_{t=1}^{n\tau} \{\xi(t) - \langle \xi \rangle_{n\tau}\}^2 \right]^{1/2} \tag{5b}$$

$$X(n\tau) = \sum_{u=1}^{n\tau} \{\xi(u) - \langle \xi \rangle_{n\tau}\} \tag{5c}$$

Then, the range R of the time series is defined by

$$R(\tau) = \max_{1 \le t \le \tau} X(t, \tau) - \min_{1 \le t \le \tau} X(t, \tau) \qquad (5d)$$

The range $R(\tau)$ then represents the maximum span that the particle has traversed, that is, the difference between the maximum position in the positive direction of the line of motion and the minimum position (maximum position in the negative direction). Hurst (1951) and Hurst et al. (1965) showed empirically that in the *absence* of long-run statistical dependency R/S should become asymptotically proportional to $(n\tau)^{1/2}$ for records generated by statistically independent processes with finite variances, and is given by

$$R/S = \left(\frac{\pi n \tau}{2}\right)^{1/2} \qquad (6)$$

Further, Mandelbrot and Wallis (1968, 1969a,b) pointed out that while in a pure random process, past and future events (such as the steps pointed out in the example) are truly uncorrelated and Eq. 6a is exactly obeyed, many natural processes are correlated to *some extent* and the "rescaled range" R/S scales with the time window of observation τ by an exponent different from 0.5, depending on the degree of correlation in the time series

$$R/S \propto \tau^H \qquad (6b)$$

The exponent H is referred to as the Hurst exponent (Hurst, 1951; Hurst et al., 1965). For processes with H in the range of (0.5, 1), the steps in the random walk are positively correlated (referred to as "persistence"), indicating thereby that the next step in the future is probabilistically favored to be in the same "direction" or "sense" as the one in the past. Similarly, a value of H in the range of (0.0, 0.5) represents a case of "antipersistence," indicating a proclivity to reverse the "direction" or "sense" of the random motion in subsequent steps. The analysis provides clues to the nature of the flow field.

For the present work, the R/S analysis was first applied to the time series of instantaneous position coordinates of the tracer particle. In performing the R/S analysis at any given experimental condition, all the trajectories (each of which was independent and representative of different times of residence of the tracer particle) were chosen and random initial points were chosen in the trajectories. Subsequently, Eqs. 5a–5d were applied to calculate the R/S values, which are plotted on a log–log plot (referred to as Pox diagrams) such as Figure 15a, for $U_l =$ 23 cm/s, S/L = 0.20. Each data point on the R/S–τ plane corresponds to a single set of position time series data of length (total time span) given by the abscissa. Note that, for clarity, only the mean value of R/S at any given value of time lag has been plotted. The standard deviation on each of the data points was below ±5%.

The R/S plot of the position time series (Figure 15a) shows a very interesting trend, in that over short timescales (representing short-length scales of motion) the trend is linear but deviates significantly into a curve after time lags of about 80 (corresponding to a timescale of about 1.6 s). Following Mandelbrot and Wallis (1968, 1969a,b), such a trend indicates the presence of strong deterministic components in the time series, on which a random component is embedded. Clearly, the *x*- and
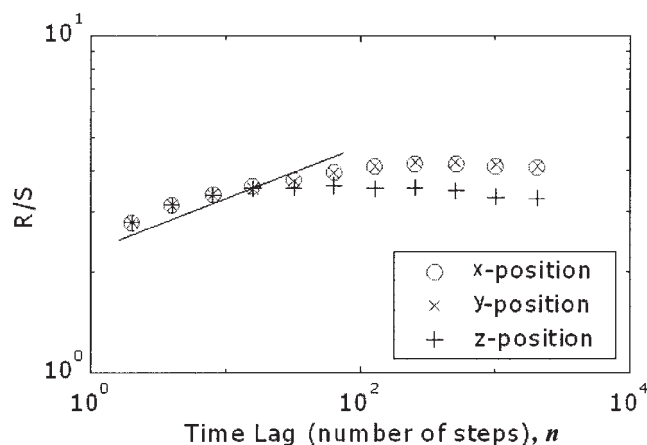
(a)
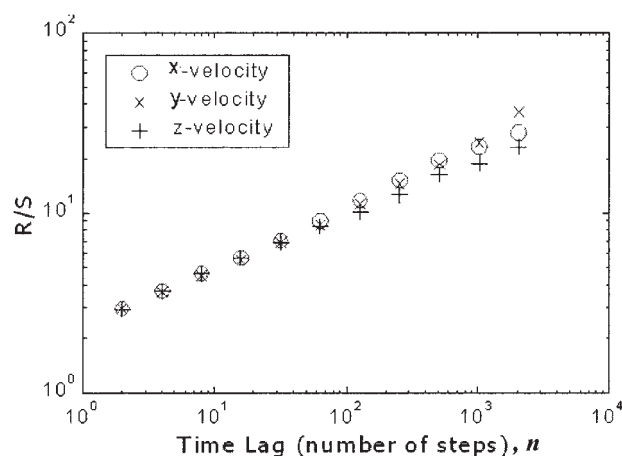
(b)

Figure 15. Pox diagrams at a typical condition of $U_l =$ 0.23 m/s, S/L = 0.20.

(a) Position time series. (b) Velocity (displacement) time series.

y-components in Figure 15a are almost coincidental, with the *z*-component showing significantly more deviation. This seems to suggest the contribution from the deterministic component of the time series is the strongest in the axial direction because strong convective currents exist in that direction and convey the solids from the inlet to the exit of the riser.

In the next stage, the Lagrangian fluctuating velocity of the tracer particle (that is, the velocity of the tracer particle as it travels along a trajectory) was inventoried to a file. This calculation was performed *after* the calculation of mean velocities (such as those shown in Figure 11a), so that the local mean velocity was subtracted from the instantaneous velocity *along the trajectory*. This exercise was performed for the entire data set, for all three components. In this manner, the fluctuating Lagrangian velocity time series of the particle was extracted,

Table 8. Hurst Exponents at Various Flow Conditions

Liquid Superficial Velocity (m/s)	Solids–Liquid Flow Ratio	x-Fluctuation	y-Fluctuation	z-Fluctuation
0.15	0.10	0.39 ± 0.03	0.41 ± 0.04	0.32 ± 0.04
0.15	0.15	0.36 ± 0.03	0.39 ± 0.01	0.33 ± 0.03
0.15	0.20	0.38 ± 0.03	0.38 ± 0.03	0.34 ± 0.02
0.20	0.10	0.38 ± 0.03	0.36 ± 0.01	0.33 ± 0.02
0.20	0.15	0.40 ± 0.02	0.37 ± 0.02	0.36 ± 0.03
0.20	0.20	0.37 ± 0.04	0.35 ± 0.01	0.35 ± 0.04
0.23	0.10	0.37 ± 0.03	0.36 ± 0.03	0.31 ± 0.02
0.23	0.15	0.38 ± 0.03	0.36 ± 0.01	0.33 ± 0.02
0.23	0.20	0.35 ± 0.03	0.35 ± 0.02	0.33 ± 0.03

and the effects of the mean velocity field were removed. Also, the time series now consists of the chain of "steps" taken by the tracer particle in its sojourn from the inlet to the exit of the riser (corresponding to a time series of "displacements" and "velocities"), rather than the "position" itself.

Again, the R/S values were calculated as before and plotted as a function of lag time. The result for the typical case of U_l = 0.23 m/s, S/L = 0.20 is shown in Figure 15b. Now, *all* three components are seen to fall on a straight line in the logarithmic plane. This indicates that, by following the Lagrangian fluctuating velocity time series, we are indeed following only the truly random components of fluctuating velocity. The results are similar to those reported by Cassanello et al. (1995) for three-phase fluidization.

Having established the existence of straight-line Pox diagrams for the displacements (velocity), the Hurst exponent was evaluated from the slope. Table 8 reports the values for the different operating conditions. Note that the reported values are representative of the *whole* flow field (because the Lagrangian velocity time series traverse the whole riser) and not necessarily any particular location in the column. All the values reported in Table 8 are below 0.5, representing a case of "antipersistent" Brownian motion of solid particles. This seems to indicate that all of the flow conditions correspond to the same flow regime, with a similar nature of dispersion of particulates. Thus, no significant variation in the Hurst exponents (which are merely "indicators" of the "nature" of dispersion) is seen among the time series recorded at the various operating conditions.

Why is the motion predominantly antipersistent? This is explained by the following physical picture: the large size and inertia of the solids result in their following one liquid eddy in one instant and being "knocked off" from that eddy in the next instant; thus, if the tracer particle (or any particle) is picked up by a large eddy at any given time instant, by the next period the particle is probabilistically favored to fall out of the eddy and

move on a different course. Indeed, such a picture of liquid–solid flow with high-inertia solid particles seems to be consistent with the observation made earlier in other multiphase systems. For example, Yang et al. (1992) reported values of Hurst exponents of up to 0.7 in bubble columns (in which the liquid was being traced), and hypothesized that this stems from the liquid motion being highly correlated with bubble flow and thus being "persistent" in nature. Cassanello et al. (1995) obtained both the persistent and the antipersistent nature of solids flow in three-phase systems.

Finally, it may be noted that it is standard practice to develop reaction engineering models for multiphase flow reactors involving a single time-averaged velocity and a dispersion coefficient. Although there is some justification for using this approach in tubular reactors and packed beds (for example, Sundaresan et al., 1980), its use in reactors in which all phases are flowing is an extrapolation not supported by much physical evidence. The discussion presented above seems to suggest that such an approach may indeed be valid. Isolation of a time-averaged flow field from the Lagrangian motion of the individual particles leaves behind a time series that can be appropriately described by Brownian motion (that is, the Pox diagrams are straight lines). How the diffusivities are to be estimated, however, is still an open question at this point and several alternative approaches may be adopted. In the remainder of this paper, we discuss this topic in greater detail.

Residence time distributions

In multiple sojourns through the riser, that is, the zone of investigation of the scintillation detectors, the tracer particle traces out the trajectories of various solid particles. In other words, it samples various trajectory realizations that are possible in the solid phase at a given operating condition. An example of three trajectories traced out by the CARPT particle is shown in Figure 16. Clearly the trajectories are of different lengths, in general, and because the instantaneous velocity fields "seen" by the tracer particle is different in each visit, the residence time in each visit is in general different.

It therefore follows that monitoring the distribution of residence times of the tracer particle in multiple visits will yield the residence time distribution of the entire phase. Indeed, interpreting residence time distribution of the solid phase in this manner is completely compatible with the primitive definition of residence time distribution $E(t)$. Instead of tracing an ensemble of fluid elements released all at the same time at the inlet, as in a conventional tracer experiment, in this case we trace multiple realizations or trajectories of the same tracer particle over a long time. If the system is stationary (at any given flow condition), this distribution (or histogram) of time of residence in multiple realizations must be the true RTD function, $E(t)$, characterizing the solids flow.

With that hypothesis, the moments of the RTD function are calculated as

$$\mu_1 \cong \frac{1}{N_{traj}} \sum_{i=1}^{N_{traj}} \Delta t_i \qquad (7a)$$

$$\sigma^2 \cong \frac{1}{N_{traj}} \sum_{i=1}^{N_{traj}} (\Delta t_i - \mu_1)^2 \qquad (7b)$$
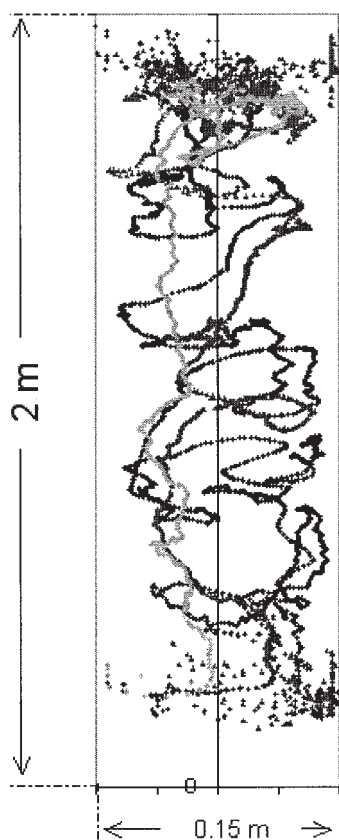
Figure 16. Three real tracks of the CARPT tracer particle in the liquid–solid riser.

U_l = 0.20 m/s; S/L = 0.10.

In the above expressions, N_{traj} is the total number of trajectories traced, Δt_i is the time duration of a trajectory as the tracer particle passes from the inlet to the exit of the riser, μ_1 is the approximation of the mean residence time, and σ^2 is the approximation of the variance. The dimensionless variance of the RTD is related to the Peclet number of the flow field, assuming a closed-closed system (Levenspiel, 1998).

Figure 17 shows histograms representing the RTD of the solid phase at typical operating conditions. All the residence time distribution curves were found to be unimodal with an extended tail, indicating that the extent of backmixing in the solid phase is significant. Table 9 lists the mean residence time, the variance, and dimensionless variance for the solid-phase RTDs obtained at each operating condition. Also listed are the parameters of a tanks-in-series and axial dispersion model that best describes the mixing patterns. Clearly, the backmixing in the solid phase is quite severe and increases both with increased liquid superficial velocity and with the S/L flow ratio. Note that these *overall* backmixing parameters reflect backmixing arising from both the convective flow profile (Figure 11) (which has a significant downflow fraction that goes up with liquid velocity and S/L ratio) and from the Lagrangian dispersion.

It is noteworthy that in dense systems such as the liquid–solid riser, measurement of solid-phase RTD by introducing an ensemble of tracer particles and monitoring their exit age distribution is impossible with normal measurement tech-

niques. Further, with the technique of sampling all possible realizations over a long enough time window of the experiment, we are ensuring that all the multitude of timescales (which typically exist in a turbulent, multiphase system) are sampled effectively so that the RTD thus deduced is indeed a reflection of the true distribution of solids residence times in the system. We are, of course, assuming that the tracer particle used in this RTD measurement follows the solids phase with fidelity (which, in any case, is an inherent approximation in the CARPT method and all the information deduced from the experiment).

It may be noted that under a similar set of conditions and on the same setup, the liquid RTD was found to have very little dispersion (Roy, 2000), from a series of conductive tracer RTD experiments. Nevertheless, the solids seem to have a very large amount of dispersion. To understand this, one notes that liquid eddies interact with solid particles depending on the energy of the eddies and the inertia of the solid particles. For very small solid particles (micron size), the liquid eddies capture the particles and carry them. For large solid particles, the eddies "slip" on them and, depending on their energies, can carry them to some distance. What probably occurs in the liquid–solid riser is that a typical energy-containing liquid eddy would catch a particle and carry it up some distance, as long as it has sufficient energy. The energy-dissipation mechanisms of liquid–solid, solid–solid, solid–wall, and liquid turbulence extract energy from the eddy. Eventually, the solid particle can no longer be carried further upward and is "shed" by the eddy, which continues its journey to the exit of the riser. The particle falls downward, hitting other particles and eddies in the process, until it meets another eddy that has sufficient energy to carry it up again. This mechanism continues until the particle finally finds its way out of the riser. Clearly, such a simplified picture would explain why the solids suffer from severe backmixing whereas the liquid backmixing is only marginal.

Trajectory length distributions

The concept for quantifying the extent of backmixing by studying the distribution of trajectory lengths (TLDs) was introduced by Villermaux (1996). A detailed description of this theory has been reported elsewhere (Roy, 2000; Villermaux, 1996); however, the key quantities that describe the distribution of trajectory lengths are as follows:
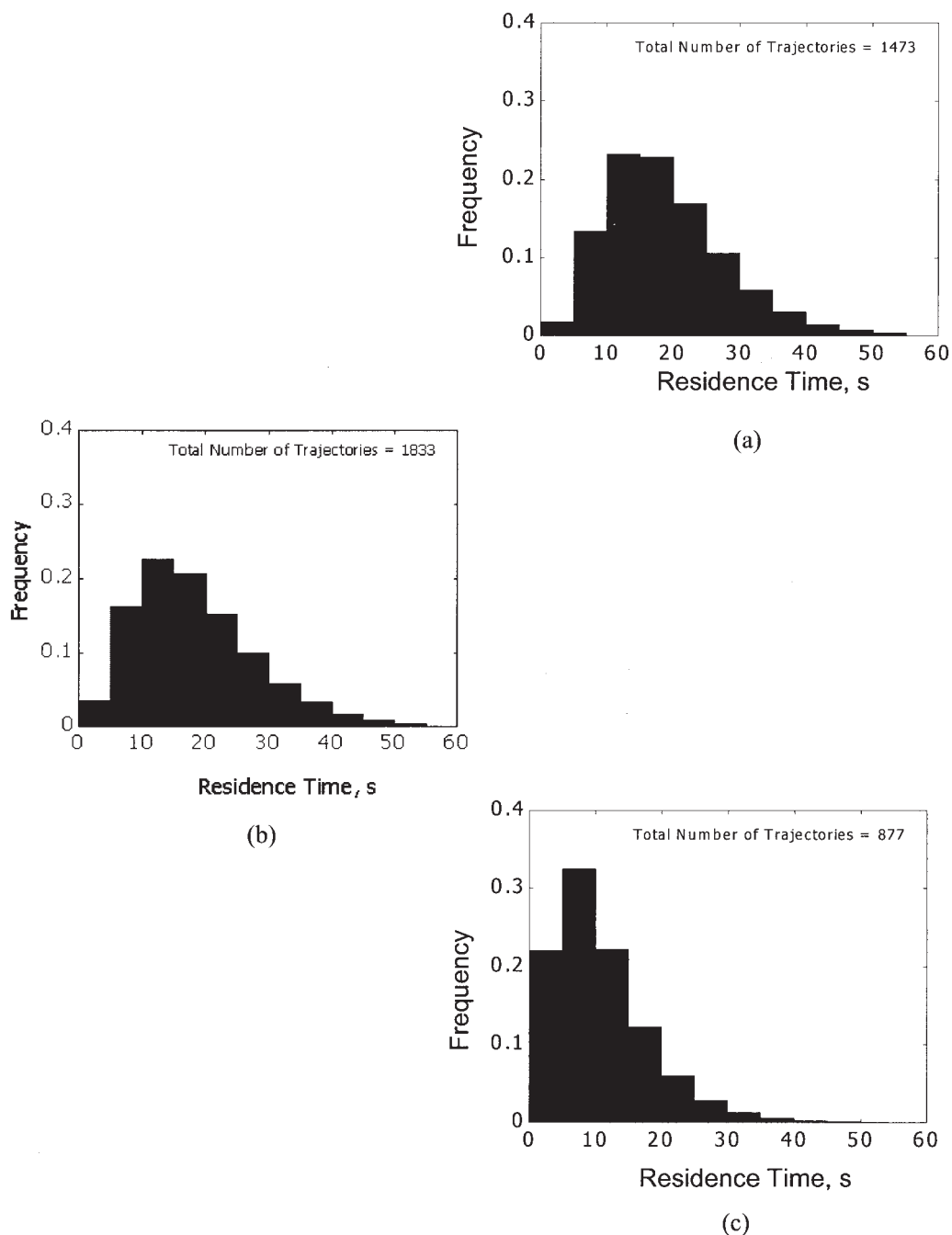
First Moment

$$\langle l \rangle = \mu_1 = \int_0^\infty l f(l) dl \tag{8a}$$

Second Moment

$$\sigma_l^2 = \int_0^\infty (l - \langle l \rangle)^2 f(l) dl = \mu_2 - \mu_1^2 \tag{8b}$$

Macromixing Index

$$M = \frac{\langle l \rangle}{L} \tag{9a}$$

Figure 17. Some typical residence time distributions calculated from CARPT data.

(a) U_l = 0.15 m/s; S/L = 0.15; (b) U_l = 0.20 m/s; S/L = 0.10; (c) U_l = 0.23 m/s; S/L = 0.20.

Dimensionless Variance

$$\sigma_{Dl}^2 = \frac{\sigma_l^2}{\langle l \rangle^2} \qquad (9b)$$

For Plug Flow

$$M = 1 \qquad \sigma_{Dl}^2 = 0 \qquad (9c)$$

For a Stirred Tank

$$M = \infty \qquad \sigma_{Dl}^2 = 1 \qquad (9d)$$

CARPT is perhaps one of the few techniques that actually allows the quantification of TLDs. In effect, this offers an alternative way to quantify backmixing, in addition to conventional RTD theory. Figure 18 shows the normalized trajectory length distributions for three typical flow conditions in the

Table 9. Mixing Parameters from Solid-Phase RTD

Liquid Superficial Velocity (m/s)	Solids-to-Liquid Flow Ratio	Mean Residence Time (s)	Variance (s^2)	Dimensionless Variance	Equivalent Number of Tanks in Series	Peclet Number for Axial Dispersion	Macromixing Index
0.15	0.10	28.3	144.2	0.18	6	10.0	2.8
0.15	0.15	23.7	129.1	0.23	5	7.5	3.4
0.15	0.20	18.8	130.8	0.37	3	4.1	4.1
0.20	0.10	19.3	108.0	0.29	4	5.7	3.9
0.20	0.15	13.2	67.9	0.39	3	3.8	5.4
0.20	0.20	12.5	95.3	0.61	2	1.7	5.9
0.23	0.10	15.5	105.7	0.44	3	3.2	5.2
0.23	0.15	12.9	64.9	0.39	3	3.8	5.6
0.23	0.20	12.1	67.3	0.46	3	2.9	6.3

liquid–solid riser. The calculations for obtaining these histograms were implemented by following *each* trajectory in the filtered CARPT raw data set and summing the segment lengths between successive positions of the tracer particle. These calculations were implemented between the fictitious planes of 0 and 1.8 m. The abscissa has been normalized by the length of 1.8 m to illustrate the distribution of trajectory length with respect to the shortest distance between the planes. The macromixing index *M* is simply the mean of this distribution.

The last column in Table 9 shows the macromixing index for the various operating conditions. The "level of backmixing" from the macromixing index is, as expected, in line with the conclusions from the dimensionless variance and Peclet number of the RTD. The macromixing index increases both with increasing the S/L flow ratio and the liquid superficial velocity, indicating that the solid phase is more backmixed under these conditions.

One could extend these concepts to study internal circulation fields from the CARPT data. If one identifies a plane of interest, then it is possible to track the trace of the CARPT tracer particle to probe *into* a trajectory and see how a typical tracer particle circulates in its sojourn from the inlet to the exit of the riser. The time the tracer particle takes to leave a plane of interest and then return to it can be termed the circulation time, and the corresponding length of trajectory traversed can be called the return length. Probability density functions of these times and lengths define the corresponding circulation time and return length distributions, respectively. These quantities allow one to explore the local circulation patterns in the riser, for example, and can be used as effective diagnostic tools for detecting dead zones, bypassing, and so forth. In the interest of conciseness, discussion of circulation times and return length distributions for the liquid–solid riser of interest is not considered here. The interested reader is advised to refer to the thesis published by Roy (2000).

Local solids dispersion

In the preceding sections, the RTD data provided information about the global backmixing in the liquid–solid riser. Such

RTD data include the effects of local solids dispersion *as well as* effects of large-scale convective flow of the solids. In addition to the global mixing of particles, the local mixing is equally important and may contribute to reactor performance, especially for fast reactions. This section discusses the dispersion at local scales.

If one were to focus attention at any given point in the liquid–solid riser and release all the particles in that unit cell at any given time, then in subsequent time steps the particles would disperse with the flow as they move out in a random manner. Dispersion is the physical quantity that characterizes the random motion of this swarm of particles. The CARPT measurement, applied to the liquid–solid riser for example, allows one to quantify the effective dispersion of the solid particles, in accordance with the work of Taylor (1921). For reasons of conciseness, the development is not presented here but the interested reader is urged to refer to the theory presented in the relevant literature (Brodkey, 1995; Degaleesan, 1997; Roy, 2000; Taylor, 1921).

In calculating diffusivities from CARPT data, one needs to establish the equivalence of the Lagrangian motion of *a single* tracer particle through any cell *over multiple trajectories* to that of many particles released from that cell *at the same time*. The concept is shown in Figure 19. At some time, if the tracer particle enters a computational cell (control volume), a counter is turned on and the particle is followed for about 200 subsequent steps. This kind of timescale has been found to be sufficiently large so that the tracer particle "forgets" its history. When the particle returns again after a long time, a new trajectory tracking is initiated. This process is repeated for the entire data set over a large number of computational cells to collect sufficient statistics. The algorithm has been described in detail by Degaleesan (1997). Thus, at the end of this process (after the entire data set has been treated), for *each* compartment one has an ensemble of trajectories that originated in that compartment. Invoking ergodicity, this ensemble of trajectories may be viewed as a swarm of particles that were released at
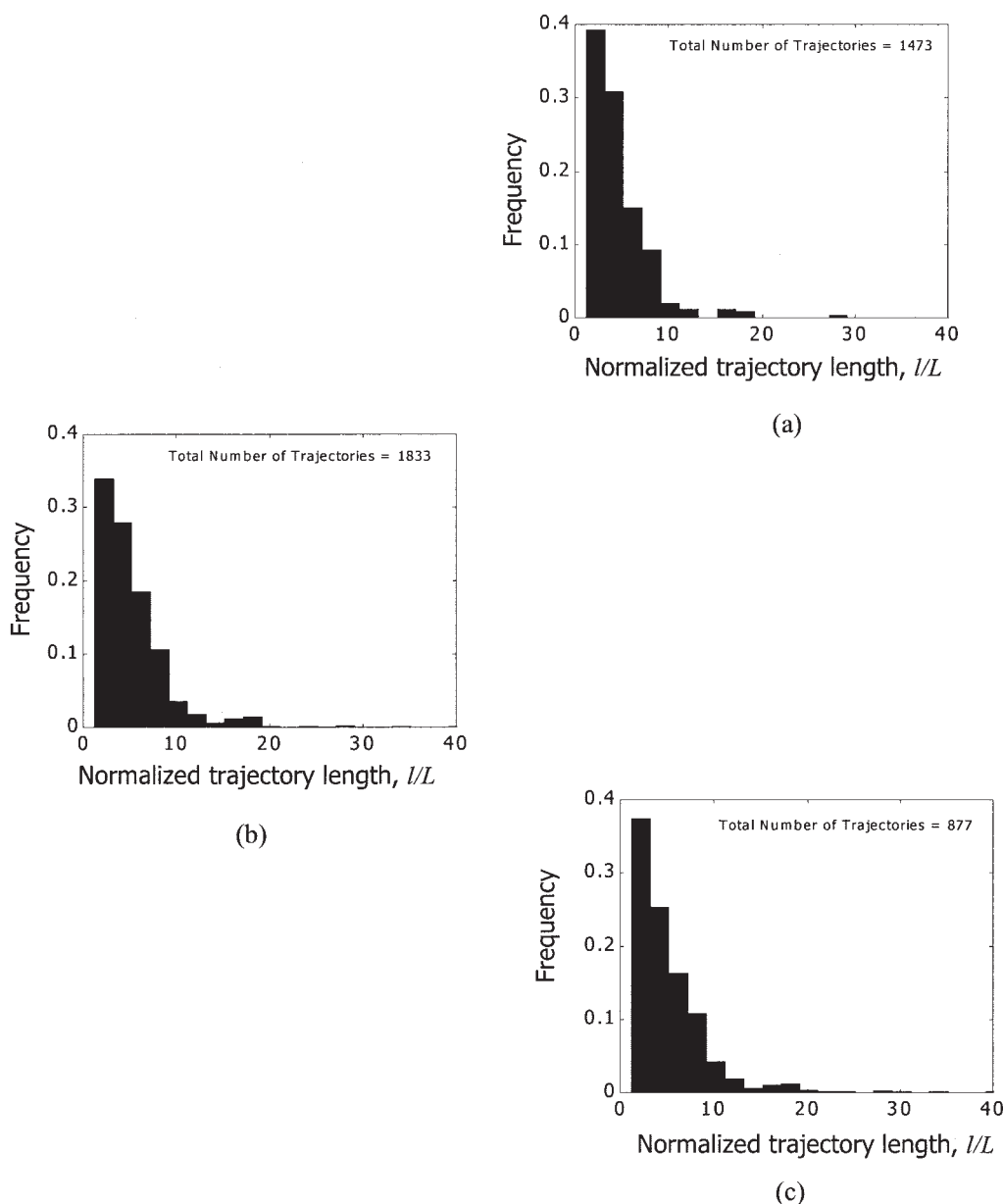
Figure 18. Some typical trajectory length distributions calculated from CARPT data.

(a) $U_l = 0.15$ m/s; S/L = 0.15; (b) $U_l = 0.20$ m/s; S/L = 0.10; (c) $U_l = 0.23$ m/s; S/L = 0.20.

some time from *that* compartment and eventually diffused out of the compartment.

One possible way of calculating the diffusivity, using the above arguments, is to directly calculate the rate of change of variance of (tracer) particle position about the mean displacement (Mostoufi and Chaouki, 1999). We found this method to be somewhat error-prone because of the derivatives and differencing involved. An alternative procedure, outlined by Degaleesan (1997), is to follow the integral approach, and evaluate the diffusivity from the autocorrelation coefficient (Table 3). The autocorrelation coefficient reflects the time over which the tracer particle (or any given particle in the solids phase) forgets its original state.

Degaleesan (1997) modified the equations of Taylor (1921), relating the autocorrelation function to the diffusivity, but accounting for the nonisotropic component of the flow, that is, when the principal convective velocity is in one direction (z) as a function of another coordinate (r). The axial diffusivity is thus given by (Degaleesan, 1997)

$$D_{zz}(\tau) = \int_0^\tau \left[\frac{\partial U_z}{\partial r} \bigg|_{Z_r(\tau')} \left(\int_0^{\tau'} v_z'(\tau) v_r'(\tau') d\tau' \right) \right]$$
$$+ \int_0^\tau v_z'(\tau') v_z'(\tau') d\tau' \quad (10a)$$

Correspondingly, the radial diffusivity (where there is no net flow) is given by
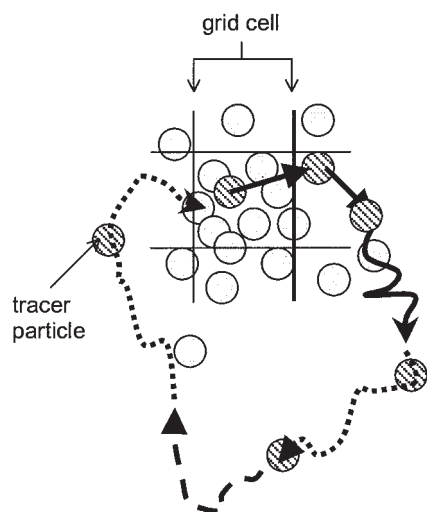
$$D_{rr}(\tau) = \int_{0}^{\tau} v'_r(\tau') v'_r(\tau') d\tau' \qquad (10b)$$

Figure 19. Schematic of particle tracing for diffusivity calculations (tracer particle shaded).

Figure 20 shows some typical plots of the autocorrelation coefficient. The functions have been scaled with their maximum value to decay from 1.0. The mean-square fluctuating velocities (that is, the maximum value of the autocorrelation function) is reported for comparison. With increasing time lag, these functions typically go to zero, representing a loss of memory of the initial state. Figure 20 shows the graphs at four different radial locations (actual calculation was performed in eight radial compartments). The statistics necessary for evaluating the autocorrelation functions are more stringent than those required for the mean velocities and turbulence quantities. Thus, the calculations were made using only the radial and axial discretization of the riser column (thus assuming axisym-
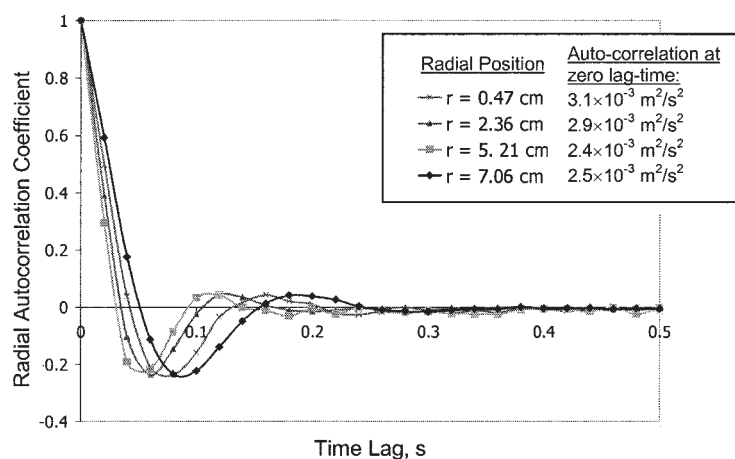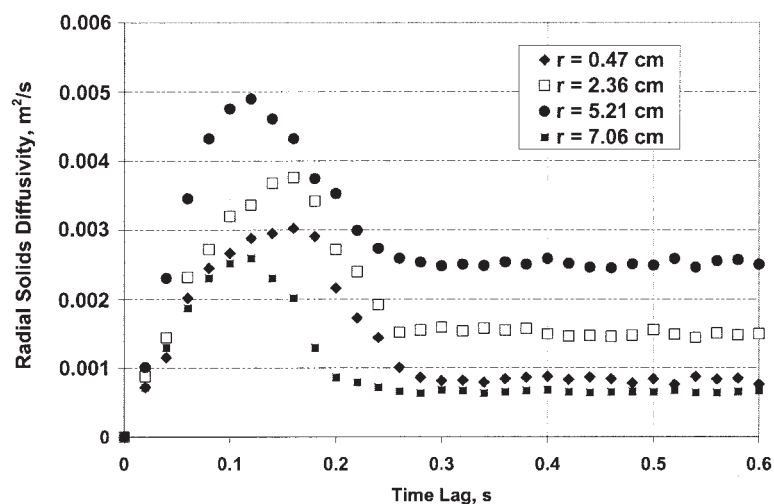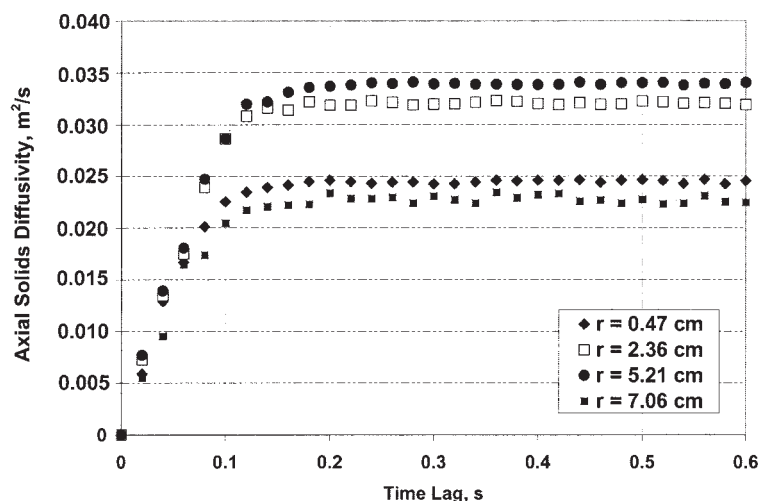

(a)
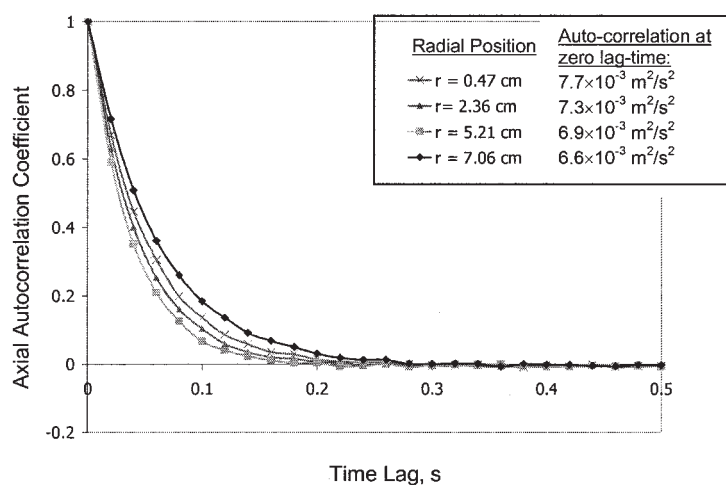
(b)

Figure 20. Autocorrelation functions for a typical case of U_l = 0.23 m/s, S/L = 0.15.

(a) Radial; (b) axial.

Figure 21. Solids diffusivities at selected radial locations, and at *z* = 0.5 m in the riser.

U_l = 0.23 m/s; S/L = 0.15: (a) radial (b) axial.

metry). The data were insufficient for proper quantification of azimuthal dependency.

Typically, two types of functional forms are seen for the autocorrelation. Figure 20a is a typical form seen in radial autocorrelation, in which the function dips below zero and then oscillates to a stationary value of zero at large times. This kind of curve is seen because the radial coordinate is limited to the wall of the riser, causing a periodic component in the decay. Thus, the tracer particle dispersing outward hits the outer wall and then disperses or "bounces back" into the riser. This leads to a kind of "negative memory" effect, characterized by negative dips in the autocorrelation function [in classical turbulence theory, such curves are characteristic of wall-bounded flows, and "necking" smoke plumes (Brodkey, 1995)]. For the *z*-component, the extent is virtually infinite and the particles near the center of the column have complete freedom to diffuse in the *z*-direction. Thus, in the *z*-direction, the diffusing particles lose memory "monotonically," and become uncorrelated with their earlier state with the autocorrelation coefficient sim-

ply decaying exponentially. Although the lack of sufficient statistics precluded accurate determination of the theta component of diffusivity, the autocorrelation of the theta-position time series should also have a form similar to Figure 20b.

Figure 21 shows typical curves of diffusivities estimated using Eqs. 10a and 10b, for a typical condition of U_l = 0.23 m/s, S/L = 0.15. The diffusivities are plotted as a *function* of the time lag because in the general case the rate of dispersion of the swarm of particles is a function of the time since the dispersion began. The radial dispersion is "quenched" by the presence of walls and is brought down to a much smaller value. The axial diffusivities grow freely to their asymptotic values for large times.

For engineering purposes, it is of interest to find a *single* representative dispersion coefficient as a function of radial position, which can be used to represent the local state of backmixing. Inherently, a single representative diffusivity (a single number, which models dispersion about plug flow) used for design and scale-up, or in convective–diffusion models, is
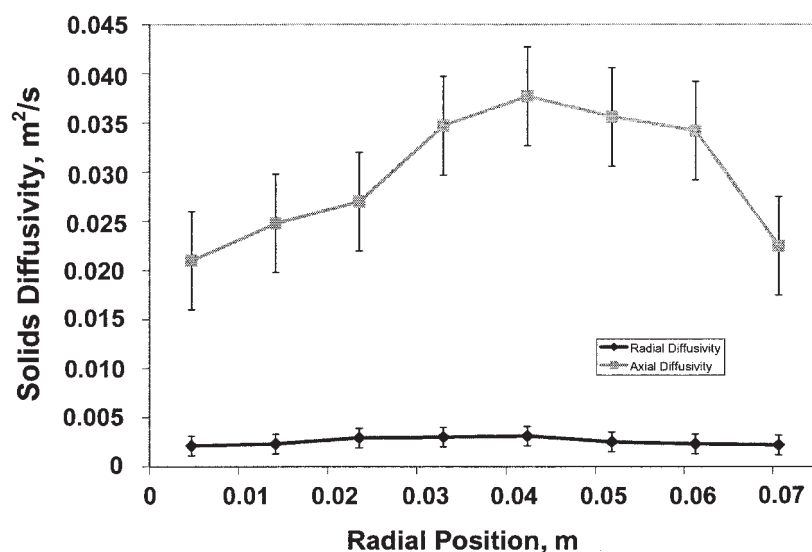
(a)
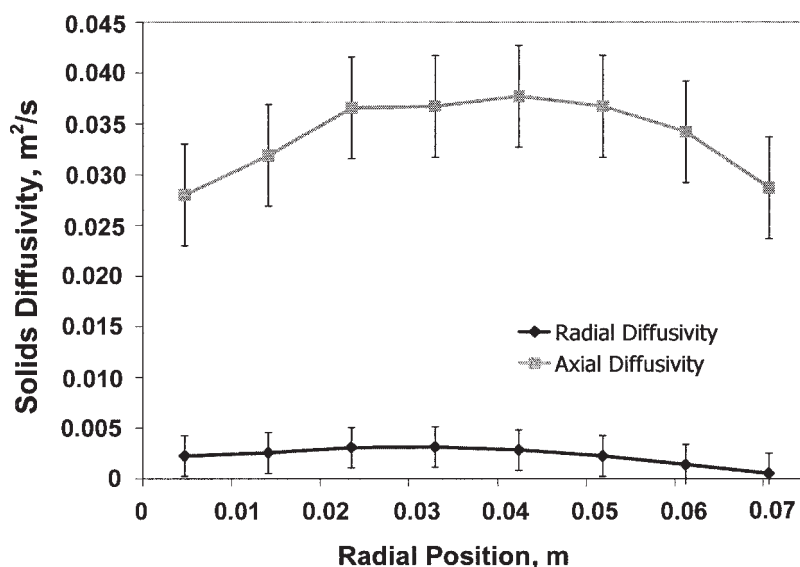
(b)

Figure 22. Asymptotic values of solids diffusivities as a function of radial position in the riser.

(a) $U_l = 0.23$ m/s, S/L $= 0.10$; (b) $U_l = 0.23$ m/s, S/L $= 0.20$.

a Eulerian quantity. However, viewed from the perspective of Taylor (1921), dispersion is inherently a Lagrangian process and is thus a function of a time lag (and spatial coordinate, with reference to the point of initiation of the swarm). How does one interpret the diffusivity (function of time lag) and choose a representative value that can be used for design, or as input parameters for typical convective–diffusion models?

It seems reasonable that, depending on the characteristic timescale of the processes that are affected by the dispersion phenomenon, one may need to choose a value that is commensurate with those timescales. For example, if a very fast reaction were being effected in a reactor vessel, then the charac-

teristic diffusivity would be evaluated at small time lags. If the reaction were very slow, then the diffusivity that really determines its rate is one that exists at large time lags.

Here, for comparison purposes, we adopt the long-time diffusivities both for the axial and the radial components. Typical radial variations are shown in Figure 22. The solids diffusivities calculated by the aforementioned method were cross-sectionally averaged to have representative eddy diffusivities at each flow condition. The results are summarized in Table 10. With increases in both solids flow rate and liquid flow rate (superficial velocity), the dispersion increases. Note that with increasing solids flow rate, the turbulent energy (and

U_l (m/s)	S/L	D_{zz} (m²/s)	D_{rr} (m²/s)	Axial Diffusivity from Dimensionless Variance of RTD (m²/s)
0.15	0.10	0.015	1.21×10^{-3}	0.017
0.15	0.15	0.026	1.87×10^{-3}	0.027
0.15	0.20	0.024	2.41×10^{-3}	0.034
0.20	0.10	0.022	1.78×10^{-3}	0.025
0.20	0.15	0.029	1.83×10^{-3}	0.044
0.20	0.20	0.039	2.54×10^{-3}	0.056
0.23	0.10	0.032	2.05×10^{-3}	0.045
0.23	0.15	0.033	2.43×10^{-3}	0.049
0.23	0.20	0.035	2.63×10^{-3}	0.059

Eulerian RMS velocities) were found to decrease slightly. Yet, the diffusivities increase significantly. Note that these quantities are, in general, based on different mean or average velocities: the RMS velocity calculation is Eulerian, whereas the diffusivity calculation is Lagrangian. Further, even though small-scale random fluctuations may decrease with increasing solids flow rate, the large-scale circulation increases (this was also seen in the discussion of internal circulation). This contributes to higher effective diffusivity. In the way in which the Lagrangian autocorrelation is calculated, the tracer particle travels out of its compartment of origin and travels into other parts of the column with the flow. Thus, the Lagrangian correlation coefficient, and thus the calculated diffusivity, senses

contributions not only from the local relatively high frequency fluctuations but also from the global mixing by large eddies (in other words, the way in which the tracer particle "spread out"). The Eulerian RMS velocities, on the other hand, are a measure of the fluctuations *in* a particular compartment, and have little to do with global backmixing. There is no Lagrangian information in their (per cell RMS velocity) calculation and interpretation, even though they are evaluated by multiple visits (in the same cell) of a tracer particle that is being *tracked* in a Lagrangian manner. Even in single-phase turbulent flow, Eulerian and Lagrangian autocorrelation coefficients have been seen to yield dissimilar behavior (Brodkey, 1995). The above discussion also indicates that the simple scaling relationships linking the Eulerian RMS velocities and diffusivities, popular in many single-phase flow situations (for example, Franz et al., 1984), are not directly suitable for high-density liquid–solid flows.

For comparison, the effective axial dispersion coefficients, calculated from the variance of the solids RTD measured with CARPT, are also listed in Table 10. Note that these dispersion coefficients are *overall* diffusivities, which include the effect of the axial, radial, and azimuthal diffusivity, as well as the overall convective backflow of solids. There is also the contribution from internal circulation at the entrance and exit of the riser, regions that have not been used (for lack of reliable data) in the diffusivity calculations reported in this section. Thus, these values of the effective axial overall diffusivities (that is, axial dispersion coefficients) are consistently higher than the axial solids diffusivities, as they should be.

If one adopts the column diameter as the characteristic length scale for radial dispersion, and the column length as the characteristic length scale of convection as well as axial dispersion (mixing), then one can estimate the characteristic times of the two processes. Table 11 reports the values for the two phenomena using the D_{zz} and D_{rr} values reported in Table 10. The axial dispersion coefficients calculated directly from the Peclet number of the solids RTD (Table 9, using the dimen-

Table 11. Characteristic Solids Mixing Times

U_l (m/s)	S/L	Characteristic Axial Convection Time (s)	Mean Residence Time from RTD (s)	Characteristic Axial Mixing Time (s)	Characteristic Radial Mixing Time (s)	Peclet Number ($= \tau_D/\tau_c$)	Peclet Number from RTD
0.15	0.10	27.5	28.3	211.5	19.6	7.7	10.0
0.15	0.15	22.4	23.7	124.5	12.7	5.6	7.5
0.15	0.20	17.6	18.8	132.0	9.8	7.5	4.1
0.20	0.10	19.1	19.3	147.5	13.3	7.7	5.7
0.20	0.15	13.4	13.2	111.6	13.0	8.3	3.8
0.20	0.20	12.6	12.5	83.9	9.3	6.7	1.7
0.23	0.10	14.9	15.5	100.2	11.6	6.7	3.2
0.23	0.15	13.6	12.9	96.9	9.8	7.1	3.8
0.23	0.20	12.3	12.1	92.0	9.0	7.5	2.9

sionless variance of the RTD) are also listed for comparison (note that the voidage or solids holdup in the column is accounted for in this calculation).

From Table 11, one observes that the characteristic convection time (calculated as the riser length divided by the mean interstitial solids velocity, or the riser volume times solids holdup divided by solids flow rate) and the mean residence times from the RTD are in good agreement. This in itself is not surprising, given that the same data (processed to the same level of complexity) were used to calculate both quantities. Thus, they should be, and are, in good agreement. The axial Peclet numbers calculated from the diffusivities calculations (defined as the ratio of these characteristic times, τ_D/τ_c) are higher in most cases, except at the lowest liquid superficial velocity, compared to those obtained from solids RTDs. Thus, the RTD seems to be accounting for more relative backmixing than the diffusivities because they contain information on radial diffusion, which also contributes to axial dispersion and which is not accounted for in our simple comparison of convection and axial diffusion times. In addition, RTDs contain the effect of severe solids backmixing at the inlet of the riser and also at the exit, which is not accounted for in the τ_D/τ_c comparison.

Summary and Conclusions

Knowledge of flow patterns and phase distributions is important in determining the performance of liquid–solid risers as chemical reactors. To assess the reactor performance, the spatial distribution of phases, velocity fields, residence time *distributions*, and backmixing should be identified. This work discusses the findings from an extensive experimental program to assess the above quantities in liquid–solid risers. Noninvasive flow-mapping techniques, such as CARPT and CT, were used and were appropriately tailored to enable the study of a system as turbulent and dense as a liquid–solid riser. In that respect, this work may be considered both an exploration into the hydrodynamics of liquid–solid flows in vertical risers and an effort to develop and demonstrate the use of reliable, noninvasive radiation-based techniques for probing such flows. Clearly, conventional methods for flow measurement, and even optical, acoustic, or electromagnetic noninvasive techniques, would have proved futile for studying such dense and turbulent two-phase flows.

The primary conclusion regarding the time-averaged solids volume fraction obtained by gamma-ray computed tomography (CT) was that the solids distribution in the riser was uniform, with some minor accumulation of solids at the walls. No discernible axial variation of solids was seen *in* the three levels (0.5 m-, 1.0 m-, and 1.5 m- elevations) at which scanning was performed. The mean cross-sectional holdup increases with increasing the solid flow rate at a fixed liquid flow rate, and decreases with increasing liquid flow rate at a fixed solids-to-liquid flow ratio. Gamma-ray tomography, as used in this work, is a suitable technique for these measurements and yielded reproducible results with good accuracy.

Our detailed experimental investigation with the computer-automated radioactive particle tracking (CARPT) showed that in a time-averaged sense, the solids were found to be flowing up at the center, having a zero axial velocity at around a dimensionless radius of 0.8, and flowing down at the wall.

Clearly, this can be viewed as large-scale convective backmixing. The histogram of the fluctuating solids velocity at any *given* point showed a near Gaussian distribution.

The radial velocity field of the solid phase indicated that the absolute magnitude of the time-averaged radial velocity was negligible compared to the axial velocity. There is no net flow in the radial direction. The root mean square (RMS) values, however, of the radial component of solids velocity and the axial component of solids velocity are of comparable magnitude. The fluctuations in the position and velocity of each solid particle are significant in either direction, even though the *mean* radial velocity is zero. At each condition the radial RMS velocity was found to be roughly half of the axial values. This seems to indicate that the fluctuating velocity field, referred to as "solids-phase turbulence" for lack of a more descriptive term, is an anisotropic field with more fluctuations in the axial direction. This in itself suggests that the dispersion of solids, which is a *Lagrangian* interpretation of velocity fluctuations in contrast to RMS velocities, which is a *Eulerian* description, would be significant in the axial direction when compared to the radial direction.

The solids-phase kinetic energy also shows similar behavior (kinetic energy being the sum of mean square velocities in the three coordinate directions). With increasing liquid superficial velocity, the fluctuating solids kinetic energy increases for a given solids-to-liquid flow ratio. At a fixed liquid superficial velocity (total flow rates of liquid at a given inlet pressure), the fluctuating solids kinetic energy is reduced slightly with increased solids-to-liquid flow ratio. This is because for the same energy input to the system (with the incoming liquid), a higher solids flow rate exists. The higher solids mean velocity field (that determines the overall solids flow rate) extracts more energy from the liquid phase, and thus the solids velocity fluctuations *at any point* are somewhat suppressed. A kinetic energy budget was performed to tabulate the distribution of flow energy in the mean and fluctuating velocity fields of the two phases. With increasing solids flux at a given liquid flow rate, the solids extract a larger fraction of the energy to support the higher mean flux and thus the intensity of fluctuations is suppressed.

Rescaled-range (*R/S*) analysis was performed with the instantaneous particle position and Lagrangian velocity fluctuation data. Both of these time series are Lagrangian, describing the solid particles flow field, except that the latter has the "influence" of the mean velocity field "extracted" out in some sense. The study revealed that the position data exhibit strong convective effects and showed "antipersistence." This means that if a given solid particle travels in a particular direction in a given time instant, then in the next time instant it is more likely to travel in the opposite direction. This seems to be a characteristic of solids particles that are denser than the liquid phase, given that because of particle inertia a particle is likely to "drop off" streamlines constantly and be swept by new eddies in the liquid phase. *R/S* analysis of the Lagrangian *velocity* data, however, revealed that the velocity *fluctuations* were close to "Brownian," that is, nearly random variable with only marginal antipersistence effects. Also, evidence of large-scale convective effects was no longer seen once the time-averaged velocity components were subtracted out from the time series. This is intuitively agreeable and suggests an important result that it is *indeed* possible to use reactor models of

first-order accuracy based on a mean flow field (representing convection) and a dispersion coefficient (lumping the random motion of *all* frequencies and origins).

Having that evidence based on reliable experimental findings, the next step was actual evaluation of the diffusion coefficients. The integral method for estimating the solids dispersion was used, that is, evaluating the autocorrelation function of position, estimating the integral timescale and subsequently the components of the diffusion coefficient tensor. This is a method strictly valid for an isotropic flow field (Taylor, 1921), and thus the modification proposed by Degaleesan (1997) was used.

The axial diffusivities were found to be of the order of 0.01–0.04 m^2/s, whereas the radial diffusivities were of the order of 0.001–0.003 m^2/s. Clearly, the larger fluctuations in the axial velocity contribute to significant *Lagrangian* motion of the particle, causing large axial dispersion. The diffusivities were found to increase both with liquid superficial velocity and with solids flow rate. Note that, as discussed earlier, increasing the flow ratio of solids to liquid actually suppressed the solids velocity fluctuations about the mean velocity. However, increased solids-to-liquid ratio still contributes to higher diffusivity, which is really a measure of how "fast" the particles "spread out" in a flow field when released from a point. Solid velocity fluctuations at a given point (the *Eulerian* view) is only one of the contributors to this phenomenon, the other being large-scale convective mixing.

An alternative way to interpret global solid-phase backmixing was by physically extracting the residence time distribution (RTD) of the solids phase. This is a novel way of calculating RTD, by actually counting the residence times of a tracer particle and then finding the p.d.f. of the ensemble of trajectories. The backmixing evaluated this way is a global quantity, and incorporates the effects of both large-scale convective flows and smaller-scale dispersion.

The related concept of trajectory length distributions, in which the actual Euclidean distance covered by the tracer particle from the entry to the exit is evaluated. Again, a p.d.f. can be formed from the ensemble of trajectory lengths. For a plug-flow reactor, this mean length of trajectory is identically equal (by definition) to the distance between the entry and the exit. In the liquid–solid riser, with an appreciable degree of backmixing, the mean length is larger. The ratio of the mean trajectory length to the physical distance between the inlet and the exit also serves as a measure of backmixing.

In summary, the work presented in this paper is an extensive and arguably the first detailed study probing into the dispersion of solids in a liquid–solid riser. Naturally, one would expect a dependency of particle size, fluid and solid properties, and scale on this behavior, which should be the subject of a future study. This work presents first results in that direction, and also lays out a methodology that can be used for such a study. In that respect, it demonstrates the use of noninvasive radiation–based techniques for probing dense, opaque multiphase flows, a situation that other techniques are ill-equipped to handle.

Acknowledgments

Notation

d_p = particle diameter, cm
g = acceleration attributed to gravity, cm s^{-2}
i = index for radial compartment; index for trajectory (Eq. 6)
j = index for azimuthal compartment
k = index for axial compartment
KE = kinetic energy per unit volume of solids, dyne cm^{-2}
N = number of independent trajectories contributing to dispersion phenomena
$N(i, j, k)$ = number of occurrences in compartment indexed by (i, j, k)
N_{traj} = number of trajectories tracked
q = index for coordinate $(r, \theta,$ or $z)$
Q_l = volumetric liquid flow rate, cm^3 s^{-1}
$\langle Q_s \rangle$ = time-averaged volumetric solids flow rate, cm^3 s^{-1}
r = radial coordinate, cm
Δr = radial compartment dimension, cm
R = radius of tube/vessel, cm
R_i = radial location of point of zero axial velocity, cm
R_{ij} = Lagrangian autocorrelation coefficient
Re_p = Reynolds number based on particle diameter
s = index for coordinate $(r, \theta,$ or $z)$
S/L = solids-to-liquid flow ratio
t = (residence) time, s
U_l = liquid superficial velocity, cm s^{-1}
v_r = radial component of solids (particle) velocity, cm s^{-1}
$\langle v_q \rangle$ = qth component of ensemble-averaged solids velocity, cm s^{-1}
$\langle v_q \rangle^{\text{RMS}}$ = qth component of RMS solids velocity, cm s^{-1}
v_q = qth component of fluctuating solids velocity, cm s^{-1}
V_θ = azimuthal component of solids (particle) velocity, cm s^{-1}
v_z = axial component of solids (particle) velocity, cm s^{-1}
$\overline{v_{z_i}}$ = time-averaged axial velocity of tracer particle in the ith trajectory, cm s^{-1}
x = spatial coordinate, cm
y = spatial coordinate, cm
z = spatial coordinate, cm
Δz = axial compartment dimension, cm

Greek letters

ε = bed voidage (= 1.0 − solids holdup)
ε_b = bed voidage (= 1.0 − solids holdup) in bulk region of a packed bed
ε_s = solids volume fraction (holdup)
ε_s = deviation in solids volume fraction (holdup) from mean
θ = azimuthal coordinate, radian
$\Delta \theta$ = azimuthal compartment dimension, radian
μ_f = viscosity of fluid, g cm^{-1} s^{-1}
μ_{eff} = effective total attenuation coefficient, cm^{-1}
μ_l = total attenuation coefficient of liquid, cm^{-1}
μ_s = total attenuation coefficient of solids, cm^{-1}
ρ_{eff} = effective mixture density, g cm^{-3}
ρ_f = fluid density, g cm^{-3}
σ_ε = standard deviation in cross-sectional average solids holdup

Literature Cited

Brodkey, R. S., *The Phenomena of Fluid Motions*, Dover Publications, New York (1995).

Carlos, C. R., and J. F. Richardson, "Solids Movement in Liquid Fluidized Beds—I: Particle Velocity Distributions," *Chem. Eng. Sci.*, **23**, 813 (1968).

Cassanello, M., F. Larachi, M.-N. Marie, C. Guy, and J. Chaouki, "Experimental Characterization of the Solid Phase Chaotic Dynamics in Three-Phase Fluidization, " *Ind. Eng. Chem. Res.*, **34**, 2971 (1995).

Chen, Y.-M., C.-S. Jang, P. Cai, and Fan, L.-S. "On the Formation and Disintegration of Particle Clusters in a Liquid–Solid Transport Bed, " *Chem. Eng. Sci.*, **46**(9), 2253 (1991).

Corma, A., and A. Martinez, "Chemistry, Catalysts and Processes for Isoparaffin Alkylation: Actual Situation and Future Trends, " *Catal. Rev. Sci. Eng.*, **35**(4), 483 (1993).

Cumberland, D. J., and R. J. Crawford, *The Packing of Particles*, Elsevier, Amsterdam (1987).

Degaleesan, S., *Fluid Dynamic Measurements and Modeling of Liquid Mixing in Bubble Columns*, DSc Thesis, Washington University, St. Louis, MO (1997).

Devanathan, N., *Investigation of Liquid Hydrodynamics in Bubble Columns via Computer Automated Radioactive Particle Tracking* (*CARPT*), DSc Thesis, Washington University, St. Louis, MO (1991).

Di Felice, R., "The Voidage Function for Fluid–Particle Interaction Systems, " *Int. J. Multiphase Flow*, **20**, 153 (1994).

Di Felice, R., "Hydrodynamics of Liquid Fluidization, " *Chem. Eng. Sci.*, **50**(8), 1213 (1995).

Dudukovic, M. P., "Tracer Methods in Chemical Reactors: Techniques and Applications, " *Chemical Reactor Design and Technology*, H. de Lasa, ed., NATP ASI Series E: No. 110, Martinus Nijhoff, Dordrecht, The Netherlands (1985).

Edmonds, T., "Oil Based Chemistry, " *Catalyst and Chemical Processes*, R. Pearce and W. R. Patterson, eds., Wiley, New York (1981).

Fan, L.-S., and C. Zhu, *Principles of Gas–Solid Flows*, Cambridge Univ. Press, Cambridge, UK (1998).

Feller, W., *An Introduction to Probability Theory and Its Applications*, Wiley, New York (1968).

Frisch, U., *Turbulence: The Legacy of A. N. Kolmogorov*, Cambridge Univ. Press, Cambridge, UK (1995).

Franz, K., T. Borner, H. J. Kantorek, and R. Buchholz, "Flow Structures in Bubble Columns, " *Ger. Chem. Eng.*, **7**, 365 (1984).

Hurst, H. E., "Long-Term Storage Capacity of Reservoirs, " *Trans. Am. Soc. Civil. Eng.*, **116**, 770 (1951).

Hurst, H. E., R. P. Black, and Y. M. Simaika, *Long Term Storage: An Experimental Study*, Constable, London (1965).

Kopko, R. J., P. Barton, and R. H. McCormick, "Hydrodynamics of Vertical Liquid–Solids Transport, " *Ind. Eng. Chem. Process Des. Dev.*, **14**(3), 264 (1975).

Kak, A. C., and M. Slaney, *Principles of Computerized Tomographic Imaging*, IEEE Press, New York (1988).

Kumar, S. B., *Computed Tomography Measurements of Void Fraction and Modeling of Flow in Bubble Columns*, PhD Dissertation, Florida Atlantic University, Boca Raton, FL (1994).

Kumar, S. B., and M. P. Dudukovic, "Computer Assisted Gamma and X-Ray Tomography: Applications to Multiphase Flow Systems, " *Non-Invasive Monitoring of Multiphase Flows*, J. Chaouki, F. Larachi, and M. P. Dudukovic, eds., p. 47, Elsevier, Amsterdam (1997).

Kwauk, M., "Generalized Fluidization: I. Steady State Motion, " *Sci. Sinica*, **12**(4), 587 (1963).

Kwauk, M., "Generalized Fluidization: II. Accelerative Motion with Steady Profiles, " *Sci. Sinica*, **13**(9), 1477 (1964).

Lange, K., and R. Carson, "E-M Reconstruction Algorithms for Emission and Transmission Tomography, " *J. Comput.-Assist. Tomogr.*, **8**(2), 306 (1984).

Larachi, F., J. Chaouki, G. Kennedy, and M. P. Dudukovic, "Radioactive Particle Tracking in Multiphase Reactors: Principles and Applications," *Non-Invasive Monitoring of Multiphase Flows*, J. Chaouki, F. Larachi, and M. P. Dudukovic, eds., p. 335, Elsevier, Amsterdam (1997).

Larachi, F., G. Kennedy, and J. Chaouki, "A Gamma-Ray Detection System for 3-D Particle Tracking in Multiphase Reactors, " *Nucl. Instrum. Methods Phys. Res. Sect. A*, **A338**, 568 (1994).

Levenspiel, O., *Chemical Reaction Engineering,* 3rd ed., Wiley, New York (1998).

Liang, W., Z. Yu, Y. Jin, Z. Wang, and Y. Wang, "Synthesis of Linear Alkylbenzene in a Liquid–Solid Circulating Fluidized Bed Reactor, " *J. Chem. Technol. Biotechnol.*, **62**(1), 98 (1995).

Liang, W., S. Zhang, J.-X. Zhu, Y. Jin, Z. Yu, and Z. Wang, "Flow Characteristics of the Liquid–Solid Circulating Fluidized Bed, " *Powder Technol.*, **90**(2), 95 (1997a).

Liang, W.-G., and J.-X. Zhu, "A Core-Annulus Model for the Radial Flow Structure in a Liquid–Solid Circulating Fluidized Bed, " *Chem. Eng. J.*, **68**(1), 51 (1997b).

Liang, W.-G., and J.-X. Zhu, "Effect of Radial Flow Non-Uniformity on the Alkylation Reaction in a Circulating Fluidized Bed (LSCFB) Reactor, " *Ind. Eng. Chem. Res.*, **36**(11), 4651 (1997c).

Liang, W.-G., J.-X. Zhu, Y. Jin, Z.-Q. Yu, Z.-W. Wang, and J. Zhou, "Radial Nonuniformity of Flow Structure in a Liquid–Solid Circulating Fluidized Bed," *Chem. Eng. Sci.*, **51**(10), 2001 (1996).

Limtrakul, S., *Hydrodynamics of Liquid Fluidized Beds and Gas–Liquid Fluidized Beds*, DSc Thesis, Washington University, St. Louis, MO (1996).

Lin, J. S., M. M. Chen, and B. T. Chao, "A Novel Radioactive Particle Tracking Facility for the Measurement of Solids Motion in Gas Fluidized Beds, " *AIChE J.*, **31**, 465 (1985).

Mandelbrot, B. B., and J. R. Wallis, "Noah, Joseph and Operational Hydrology, " *Water Resour. Res.*, **4**, 909 (1968).

Mandelbrot, B. B., and J. R. Wallis, "Computer Experiments with Fractional Gaussian Noises. Part 1. Averages and Variances, " *Water Resour. Res.*, **5**, 228 (1969a).

Mandelbrot, B. B., and J. R. Wallis, "Computer Experiments with Fractional Gaussian Noises. Part 2. Rescaled Ranges and Spectra, " *Water Resour. Res.*, **5**, 242 (1969b).

Miller, A., and D. Gidaspow, "Dense, Vertical Gas–Solid Flow in a Pipe, " *AIChE J.*, **38**, 1801 (1992).

Moustofi, N., and J. Chaouki, "Local Solids Mixing in Gas–Solid Fluidized Beds, " *Powder Technol.*, **114**(1–3), 23 (2001).

Nauman, E. B., and B. A. Buffham, *Mixing in Continuous Flow Systems*, Wiley, New York (1983).

Nouri, J. M., J. H. Whitelaw, and M. Yianneskis, "Particle Motion and Turbulence in Dense Two-Phase Flows," *Int. J. Heat Mass Transfer*, **13**, 729 (1987).

Roy, S., *Quantification of Two-Phase Flow in Liquid–Solid Rises*, DSc Thesis, Washington University, St. Louis, MO (2000).

Roy, S., and M. P. Dudukovic, "Flow Mapping and Modeling of Liquid–Solid Risers," *Ind. Eng. Chem. Res.*, **40**, 5440 (2001b).

Roy, S., A. Kemoun, M. H. Al-Dahhan, and M. P. Dudukovic, "A Method for Estimating the Solids Circulation Rate in a Closed-Loop Circulating Fluidized Bed, " *Powder Technol.*, **121**, 213 (2001a).

Roy, S., F. Larachi, M. H. Al-Dahhan, and M. P. Dudukovic, "Optimal Design of Radioactive Particle Tracking Experiments for Flow Mapping in Opaque Multiphase Reactors, " *Appl. Radiat. Isot.*, **56**, 493 (2002).

Sundaresan, S., N. R. Amundson, and R. Aris, "Observations on Fixed-Bed Dispersion Models: The Role of the Interstitial Fluid, " *AIChE J.*, **26**, 529 (1980).

Taylor, G. I., "Diffusion by Continuous Movements," *Proc. London Math. Soc.,* **20**, 196 (1921).

Tennekes, H., and J. L. Lumley, *A First Course in Turbulence*, MIT Press, Cambridge, MA (1972).

Thomas, C. L., *Catalytic Processes and Proven Catalysts*, Academic Press, New York (1970).

Tsoulfanidis, N., *Measurement and Detection of Radiation*, Hemisphere Publishing, Washington, DC (1983).

Villermaux, J., "Trajectory Length Distribution (TLD), a Novel Concept to Characterize Mixing in Flow Systems, " *Chem. Eng. Sci.*, **51**, 1939 (1996).

Vora, B., P. Pujado, T. Imai, and T. Fritsch, "Production of Detergent Olefins and Linear Alkylbenzenes, " *Chem. Ind.*, March (1990).

Weitkamp, J., *Catalysis by Zeolites*, B. Imelik et al., eds., Elsevier, Amsterdam (1980).

Yang, Y. B., N. Devanathan, and M. P. Dudukovic, "Liquid Backmixing in Bubble Columns via Computer Automated Radioactive Particle Tracking (CARPT), " *Chem. Eng. Sci.*, **47**, 2859 (1992).

Zheng, Y., and J. X. Zhu, "The Onset Velocity of a Liquid–Solid Circulating Fluidized Bed, " *Powder Technol.*, **114**(1–3), 244 (2001).